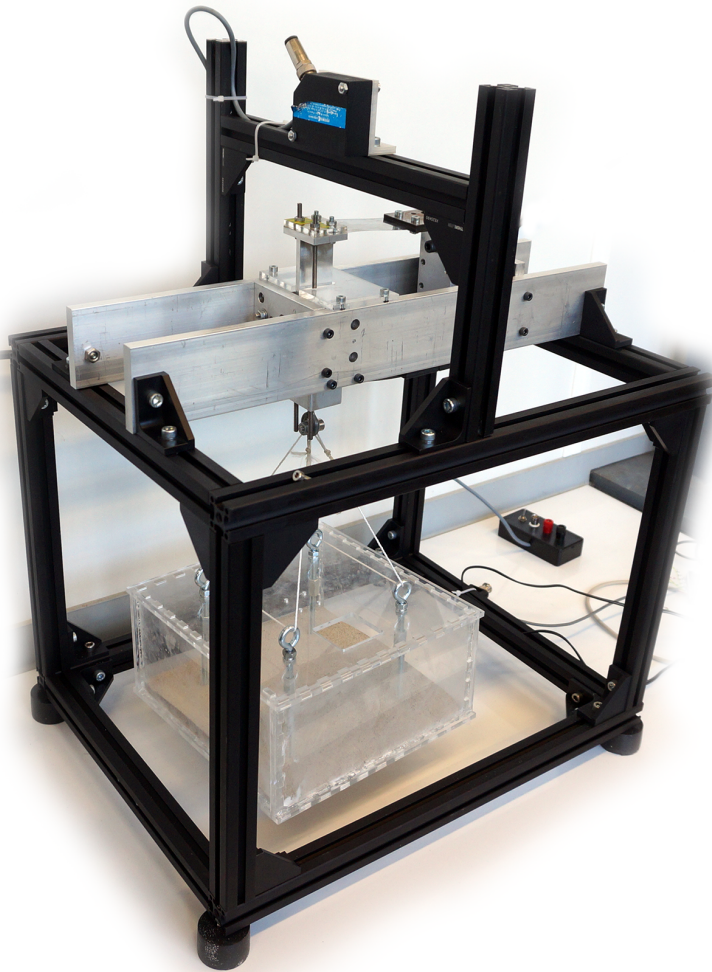


Department of Precision and Microsystems Engineering

Vertical vibration isolation using permanent magnets

Rens Berkhof

Report no : MSD 2015.010
Coach : ir. J.W. Spronck
Professor : Prof. dr. ir. J.L. Herder
Specialisation : Mechatronic System Design
Type of report : Master Thesis
Date : June 17th, 2015



Vertical vibration isolation using permanent magnets

Rens Berkhof

June 4, 2015

Summary

Ground vibrations result in disturbance forces in mechanical systems and cause position errors. High resolution imaging systems or chip fabrication machines require a high position accuracy, creating the need for vibration isolation systems. This thesis is focused on the development of a new kind of vibration isolation systems, that carries its load by means of a passive magnetic configuration called the *"magnetic gravity compensator"*. A literature study suggested that magnetic configurations with great vibration isolation properties could be made, and that passive mechanical vibration isolation systems offer the best vibration isolation performance commercially available. The goal of this research is to combine both and *"Design a passive magnetic gravity compensator, implemented in a vibration isolation system with a sub-hertz eigenfrequency"*.

A vibration isolation system requires a low-stiffness suspension of its vibration isolated platform. This low stiffness configuration is called the gravity compensator. It was found that a configuration of three square 20x20x5 mm magnets can be used to create a gravity compensator with a low stiffness range approximately equal to 1/2 of the magnets dimensions. The load bearing capacity of this gravity compensator was measured at 26 N, while its stiffness was lower than ± 200 N/m over a range of 10 mm.

Levitation of permanent magnets is not possible without the use of active control, because there is always an unstable degree of freedom. The magnetic gravity compensator was found to be unstable for one translation and one rotation, creating the need for a linear guide. COMSOL simulations showed that by tilting two of the magnets of the gravity compensator, its stiffness could be adjusted from ~ 0 N/m to ± 1000 N/m, making it possible compensate for the stiffness that a linear guide would add to the system. These same simulations showed that the load bearing capacity of the gravity compensator could be adjusted with 10 N by changing the airgaps between the magnets, while still remaining a low stiffness range of multiple millimeters.

Calculating the force-displacement curve of the magnetic gravity compensator with FEM software is a computational intensive task, and it can take multiple hours to calculate a complete curve at a high resolution. Because of the simple geometry of the rectangular magnets and the lack of iron in the concept, it is possible to derive analytical equations. One- and two-dimensional equations for the field have been derived and validated, while three-dimensional solutions have been found in literature, but where not used in this research.

The passive magnetic gravity compensator is implemented in the vibration isolation system shown in figure 1. Two leafsprings with a combined stiffness of 61 N/m are used as linear guide, to compensate for the instabilities of the magnetic concept. An eigenfrequency of 0.78 Hz is measured for vibrations up to 1 mm. When the amplitude of vibration increases to 2 mm, the eigenfrequency increases to 1.17 Hz due to the nonlinear stiffness of the setup. During these measurements the demonstrator carried a weight of approximately 25 N. The demonstrator has a high damping ratio, which is measured at 0.6 and is caused by a combination of eddy current

damping in the aluminum and material damping in the linear guide. Due to this damping, the system has relatively high transmissibility despite its low eigenfrequency when compared to other high end vibration isolation systems.

The research can be called a success in that a stable passive magnetic gravity compensator with a sub-hertz eigenfrequency is build and validated. However, there is still room for improvement. Different material choices can reduce the damping ratio drastically, while lowering the stiffness and increasing the range of this low stiffness area. A subsequent research is advised to implement these material changes and validate the tunability of the stiffness of the gravity compensator with measurements.

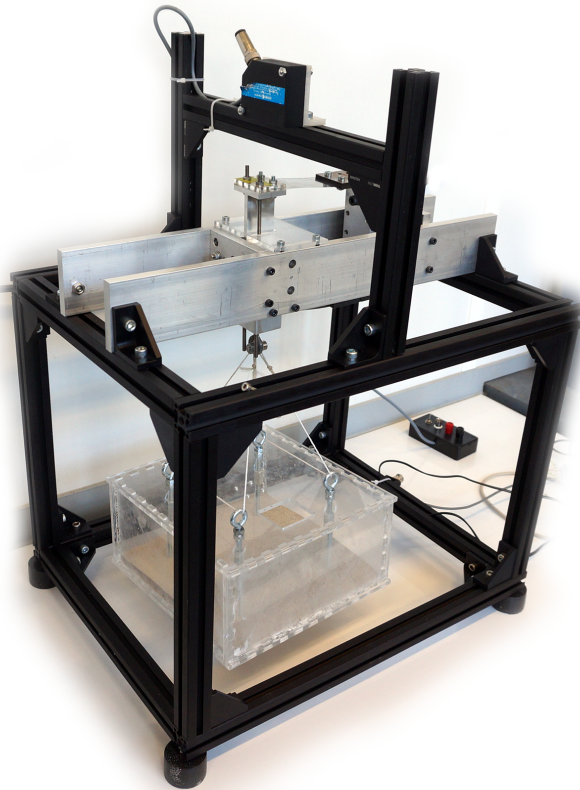


Figure 1: Photograph of the vibration isolation system. The aluminum parts contain the gravity compensator, and the plexiglass box is the vibration isolated platform. Sand is used as load.

Preface

After a year of work, I am very happy to present you my master's thesis. Last year was I journey that I will never forget. It started all when I walked into Jo's office one year ago with the message that I liked magnetism and had heard that he was the person that I had to talk to. And although I have not used a single drop of ferrofluid in my complete thesis, Jo was definitely the right person to go to.

I would not say that my thesis consists completely out of ups, there where enough downs. The moments when a COMSOL simulation crashed after hours of simulation, a laptop breaks down, or magnets that snap together and destroy themselves or the nice leafsprings that I just produced, ruined many a afternoon. And don't get me started on the sounds of 3D printers... However, that is how you learn. Up front, I would have never expected to learn this much during just one year. And for that, I would like to thank a lot of persons.

Acknowledgments

First and foremost I would like to thank Jo. There are probably no two persons that work more differently than we do, but there is also not a person at this university with more interesting ideas about magnetism than you do. Without you, I would have never made it to the finish line and I would like to thank you for that. The MSD group is a unique one in how close and collaborative it is. Charlie, Gihin, Pjotr, Ruud, Paul, Arjan, Oscar, Johan, Ruijung, Arjan, Erik, Floris, Haris, Ruud, Bart, Martijn and everybody I am forgetting: thanks for all your advice and feedback. But most of all: thank you for all the pleasant lunches, coffee brakes and bad jokes. I would also like to thank Jos van Driel for helping me with all my sensor and LabView problems, Rob Luttjeboer for all the lab supplies and Gerard and Rene for teaching me how to produce all the parts.

At last, but certainly not least, I would like to thank my parents, my grandparents, my uncle and my girlfriend for their endless support throughout the years.

Delft, June 3th 2015

Rens Berkhof

Contents

Contents	vii
Nomenclature	xi
1 Introduction	1
1.1 Background	1
1.2 Research goals and objectives	1
1.3 Structure of this thesis	2
Reading advice	2
I Theory	3
2 Vibration Isolation	5
2.1 Position accuracy and vibrations	5
2.2 Vibration isolation and transmissibility	6
Transmissibility	8
2.3 Commercial vibration isolation systems and their performance	8
Passive pneumatic vibration isolation system	8
Mechanical vibration isolation systems	9
Active vibration isolation systems	10
2.4 The passive magnetic vertical vibration isolation system	10
2.5 Amplitude of vibrations in different environments	11
2.6 Conclusions	12
3 Magnetism, magnets and magnetic forces	13
3.1 Electromagnetism and magnetostatics	13
Fields in matter	14
3.2 Magnetic dipole moment and magnetization	15
3.3 Permanent magnets and magnetic materials	15
The hysteresis loop and coercivity	17
3.4 Magnetic forces	17
3.5 Calculating forces in systems with a well defined flux path	18
Magnetic circuit theory	18
The energy balance	20
The Lorentz equation	21
3.6 Calculating forces in systems with a undefined flux path	21
The charge model	22
The current model	23
1D solution for the field of rectangular magnets	24

2D solution of the field of rectangular magnet	24
3D solution of the field of a rectangular magnet	25
Force interaction between magnets	25
3.7 Conclusion	25
II Magnetic gravity compensator design and validation	27
4 Magnetic gravity compensator concepts	29
4.1 Requirements of the magnetic system	29
4.2 Overview and discussion of concepts	30
The iron mover	30
The Halbach array	32
Attraction and repulsion	33
Square magnets	34
Magnetic concept choice	35
4.3 Extending the square magnet concept	35
Tunability	36
Tuning the load bearing capacity	36
Tuning the stiffness	38
4.4 Stability of the gravity compensator concept in all DOF	38
Translational stability	39
Rotational stability	39
Earnshaws Law	40
4.5 Influence of alignment errors or non-symmetries	40
4.6 Conclusion	42
5 Gravity compensator validation	43
5.1 Validating the B-field of a square magnet	43
Fitting the flux B-field measurements	43
5.2 Validating the force-displacement curve	44
Description of the measurement setup	44
Force-displacement curve for $\alpha = 0$	45
Force-deflection curve for $\alpha \neq 0$	47
5.3 Conclusion	47
III Demonstrator design and performance evaluation	49
6 Demonstrator design and performance evaluation	51
6.1 Functions and requirements of the demonstrator	51
6.2 Design of the demonstrator	52
Platform position	53
Linear guides	53
Positioning the magnets	54
6.3 Static force measurements	56
Tuning the stiffness	57
Hysteresis	59
6.4 Dynamic measurements	59

Eigenfrequency	59
Eigenfrequency pendulum	60
Eddy Current damping	61
6.5 Transmissibility	62
6.6 Conclusions on the demonstrator	62
7 Conclusions and recommendations	65
7.1 Conclusions	65
7.2 Recommendations for further research	66
Bibliography	67
Appendices	69
A Linear guides: calculation and validation	71
A.1 Linear guide stiffness	71
Measuring the force-displacement curve	72
Measuring the eigenfrequency	72
Damping coefficient	73
Conclusion	73
B Description of the FEM model	75
B.1 Geometry of the airbox	75
B.2 Mesh	76

Nomenclature

Roman Symbols

\mathcal{F}	Magnetomotive force [A]
\mathcal{R}	Reluctance [A/(T·m)]
\mathbf{B}	Magnetic flux density, also referred to as magnetic field [T]
\mathbf{E}	Electric field [N/C] or [V/m]
\mathbf{H}	magnetic field intensity (mechanics) or auxiliary field (physics) [A/m]
\mathbf{J}	Volume current density [A/m ²]
\mathbf{J}	Volume current density [A/m ²]
\mathbf{j}	Surface current density [A/m]
\mathbf{M}	Magnetization [A/m]
\mathbf{m}	Magnetic dipole moment [A·m]
\mathbf{V}	Force [N]
\mathbf{v}	Velocity [m/s]
A	Magnetic vector potential
B_r	Remanent flux density [T]
c	Damping [kg/s] or [N/(m/s)]
f_n	eigenfrequency of a system [Hz]
K	Surface current density [A/m]
k	Stiffness [N/m]
m	mass [kg], also used to refer to a specific magnet (m_1, m_2, m_3)
N	Primarily used to indicate the number of windings of a coil [-]
Q	Charge [C]
T	Transmissibility [-]
W'_{fld}	Coenergy stored in a magnetic field [J]
W_{fld}	Energy stored in a magnetic field [J]
I	Current [A]

Abbreviations

FEM	Finite Element Method
HVAC	Heating, Ventilating and Air-Conditioning
MEMS	Micro Electro Mechanical System

Greek Symbols

ϵ_0	Permittivity of free space [F/m]
γ	loss factor due to stray flux in a magnetic circuit
λ	Magnetic flux linkage [Wb] or [T·m ²]
μ_0	Permeability of free space, [$4\pi \cdot 10^{-7}$ T·m/A]
ω	Frequency of vibration [rad/s]
ω_n	eigenfrequency of a system [rad/s]
ϕ	Magnetic Flux [Wb] or [T·m ²]
ρ	Charge density [C/m ³]
ρ_m	Volume charge density [A/m ²]
σ_m	Surface charge density [A/m]
ϵ	Position error [m]
φ_m	Magnetic scalar potential
ξ_m	Magnetic susceptibility [-]
ζ	Damping ratio or fraction of critical damping [-]
R	radius [m]

Introduction

1.1 Background

Technology is getting smaller. Due to the current trend of miniaturization of devices, we need an increased position accuracy in the high tech machines that make these devices. Because we continue to work on smaller and smaller scales, the influence of external disturbances is increasing. Disturbance sources that were of no importance in the past can be no longer neglected and need to be taken into account in the design, or removed from the operating environment. When talking about disturbances one should think of acoustic vibrations, thermal deformations and ground vibrations. The latter is the topic of this thesis.

Ground vibrations exist in all environments throughout the world and have a variety sources, from the movement of tectonic plates, waves crashing on the shore and wind, to man made sources such as traffic, machinery and HVAC systems¹[1]. These vibrations cause disturbance forces in mechanical systems and need to be removed, when a high position accuracy is required. This happens by means of so-called vibration isolation systems, which can be built both as active or passive systems. Active vibration isolation systems make use of sensors, actuators and control to dampen vibrations, while passive systems use compliant pneumatic or mechanical springs. Both active and passive systems that can reduce vibrations by two orders of magnitude at 10Hz are commercially available. These kind of reductions in vibrations can only be achieved when the isolation system has a very low eigenfrequency and contains little damping.

This research investigates if it is possible to create a passive—magnet based—vibration isolation system that combines the strengths of the active magnetic systems with those of the passive mechanical systems, creating some sort of hybrid system. There has been significant amount of research into actively controlled electromagnetic vibration isolation systems, but a passive magnetic solution could not be found in literature [2, 3, 4, 5, 6, 7].

1.2 Research goals and objectives

The goal of this research is to *“Design a passive magnetic gravity compensator, implemented in a vibration isolation system with a sub-hertz eigenfrequency”*. The term ‘gravity compensator’ is used to indicate the part of the setup that delivers the load bearing capacity and can be thought of as a low stiffness magnetic spring. The vibration isolation system is the complete system in which the magnetic gravity compensator is used.

Designing a magnetic gravity compensator requires knowledge of electromagnetism and the tools available to evaluate the performance of magnetic systems. Obtaining, reviewing and summarizing this knowledge is an important objective of this research. Applying this knowledge to create, simulate and measure the performance of magnetic concepts is a second objective of

¹Abbreviation: Heating, Ventilating and Air-Conditioning.

this research. The final objective of this research is the production of a demonstrator that can be used to prove the achievement of my goal by measurements.

1.3 Structure of this thesis

This thesis can be split up in three parts. The first part consists of chapter 2 and chapter 3 and is mostly about the theory on magnetic vibration isolation. Chapter 2 provides an overview of the theory on vibration isolation and the working principles of commercial vibration isolation systems. Chapter 3 is a dissertation on magnetism and magnetic forces and the tools available to predict these fields and forces.

The second part of this thesis consists of chapter 4 and chapter 5 and is concerned with the design and validation of the magnetic gravity compensator. This magnetic gravity compensator is the part of the vibration isolation system that provides the load bearing capacity. Multiple magnetic concepts will be discussed in chapter 4, while chapter 5 discusses the measured performance of the most promising concept.

The last two chapters of this thesis are on the design and evaluation of the demonstrator. Chapter 6 discusses the design of the demonstrator and presents its measured performance. The conclusions and recommendations resulting from the research are presented in chapter 7.

Reading advice

This report is written in such a way that a possible successor has all the information needed to duplicate my research. A significant amount of theory is included to save this theoretical successor a lot of time searching for the right documentation, but this theory is quite in-dept. I would advice the time-conscious reader to focus of the second and third part of this research and just read the introductions and conclusions of the other chapters. This should be sufficient to follow the red-line of the story.

Part I
Theory

Vibration Isolation

The introduction of this thesis stated that the goal of this research is to “*Design a passive magnetic gravity compensator, implemented in a vibration isolation system with a sub-hertz eigenfrequency*”. It was mentioned that vibrations reduce the position accuracy of a system and therefore should be removed, using a vibration isolation system. Why vibrations result in positioning errors and how such a vibration isolation system works, is discussed in this chapter. Finally, this chapter reviews the working principle of a number of different commercial systems and the to-be-designed passive magnetic system.

2.1 Position accuracy and vibrations

There are many mechanical systems where the *relative position accuracy* of the components is of importance. Think for example of the microscope shown in figure 2.1. The lens of the microscope has a certain focus point, in which we need to place the object in order to obtain a clear image. This is done by moving the head (mass m) up and down using a spindle. This spindle assembly is not infinitely stiff and is therefore modeled as a spring. This finite stiffness causes a problem: we want a constant distance between the object and the lens to maintain a clear image, but the spring will deform when the force acting on it changes. And this changing force occurs when the base vibrates.

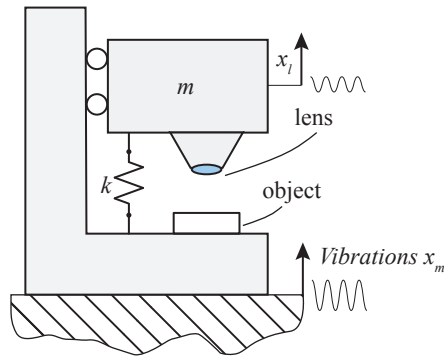


Figure 2.1: A microscope consisting of a frame on which the object lies and a head containing the lens. Vibrations cause a changing relative position of the head with respect to the object, due to the finite stiffness k . When vibrations are large and k is small, this results in a blurry image. Adapted from [8]

When the base is vibrating with a sinusoidal movement $x_m(t) = \hat{x}_m \sin(\omega t)$, the object follows that motion. Because we want a constant distance between the lens and the object, the head should follow the vibration either. To do so, the had needs an acceleration equal to [8]:

$$\ddot{x}_t = -\hat{x}_m \omega^2 \sin(\omega t) \quad (2.1)$$

Because the head is only supported by a spring, the force acting on this spring is equal to:

$$\begin{aligned} F(t) &= m\ddot{x}_l \\ &= -m\hat{x}_m\omega^2 \sin(\omega t) \end{aligned} \quad (2.2)$$

and has an amplitude of $\hat{F} = -m\hat{x}_m\omega^2$. This force deforms the spring with an amplitude of:

$$\hat{x}_l = \frac{m\hat{x}_m\omega^2}{k} \quad (2.3)$$

This equation can be further compacted by introducing the eigenfrequency of the system:

$$\omega_n = \sqrt{\frac{k}{m}} \quad (2.4)$$

Substitution of this equation into equation (2.3) results in:

$$\hat{x}_l = \hat{x}_m \frac{\omega^2}{\omega_n^2} \quad (2.5)$$

The deformation of this spring is equal to the change in distance between the lens and the object and is the position error ε . This error limits the position accuracy of the microscope. In case of a microscope, the position error could result in a blurry image when becoming too large. In case of a chip or MEMS production process, this could mean the loss of a batch of chips or MEMS devices.

According to equation (2.5), there are two ways we can decrease the position error of a system: we can increase the eigenfrequency ω_n of the system or we can decrease the amplitude \hat{x}_m of the floor vibrations. The latter is done using a vibration isolation system.

2.2 Vibration isolation and transmissibility

When a mass is suspended by some construction, a certain portion of the floor vibrations will be transferred from the floor to the mass through this construction. The goal of a vibration isolation system is to minimize the coupling between the motion of the ground x_f and the motion of the mass x_m . This coupling is called the transmissibility T and is defined as:

$$\text{transmissibility} = \frac{x_m}{x_f} \quad (2.6)$$

We can model a vibration isolation system as the mass-spring-damper system shown in figure 2.2, where k is the stiffness of the suspension and c is the damping of the suspension.

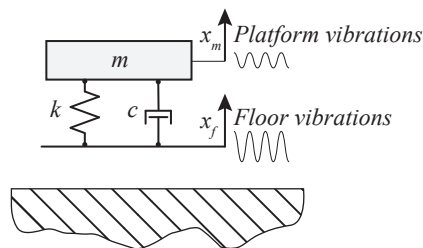


Figure 2.2: A mass-spring-damper model of a vibration isolation system. The mass is supported by a spring with stiffness k and a damper with damping c . The ratio x_m/x_f is called the transmissibility. Reproduced from [8].

The dynamics of the mass-spring-damper system are described by the following transfer function:

$$\frac{x_m}{x_f} = \frac{cs + k}{ms^2 + cs + k} \quad (2.7)$$

where s is the Laplace operator. When analyzing the performance of a vibration isolation system, it is convenient to introduce the damping ratio ζ , which is defined as:

$$\zeta = \frac{c}{2\sqrt{km}} \quad (2.8)$$

The damping ratio is also referred to as the *fraction of critical damping* and is a dimensionless number that gives the relations between the damping c and the critical damping c_r [8]. Substitution of the eigenfrequency and damping ratio and using $s = i\omega$ allows us to rewrite equation (2.7) as:

$$\frac{x_m}{x_f} = \frac{2j\zeta\frac{\omega}{\omega_n} + 1}{-\frac{\omega^2}{\omega_n^2} + 2j\zeta\frac{\omega}{\omega_n} + 1} \quad (2.9)$$

where ω is the frequency of the vibration acting on the system. Figure 2.3 shows the result of equation (2.9) for different eigenfrequencies ω_n and damping ratio ζ . From this figure we can see that for $\omega > \omega_n$, a reduction in the eigenfrequency results in a reduction in the transmissibility, and an increase in the damping ratio results in a higher transmissibility. However, below and—especially—at the eigenfrequency, the transmissibility is actually lower when the damping ratio ζ is higher. This results in a contradiction regarding the damping ratio.

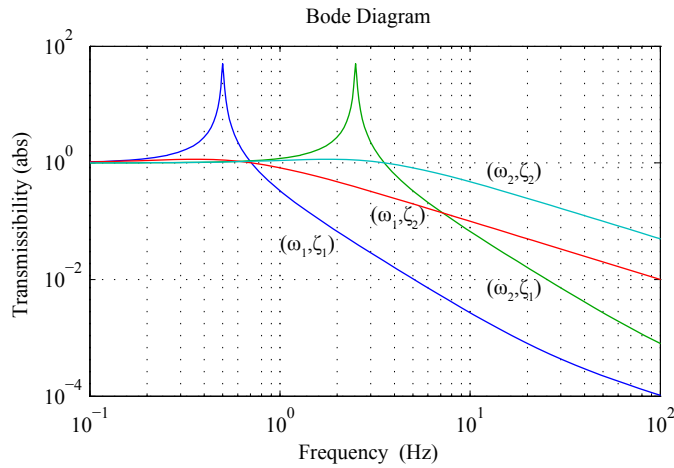


Figure 2.3: The transmissibility of the mass-spring-damper system of figure 2.2 for $\omega_i = \{0.5, 2.5\} \cdot 2\pi$ and $\zeta_i = \{0.01, 1\}$. A lower eigenfrequency and less damping results in better vibration isolation above the eigenfrequency. The peak in transmissibility indicates the eigenfrequency of the system [9, 8]

This contradiction can be solved by remembering that the purpose of a vibration isolation system is to minimize the position errors within the system placed on top of the isolation system, for instance the microscope of figure 2.1 on page 5. The position error in the microscope increased quadratically with the frequency of vibration ω and linearly with the amplitude of vibration \hat{x}_m (see 2.5 on the preceding page). Therefore we would rather lower the amplitude of vibrations at high frequencies than at low frequencies. We can conclude that a passive vibration isolation system should have an extremely low eigenfrequency and should contain little damping, approaching the ideal of a floating mass.

The low eigenfrequency can be achieved by increasing the mass or lowering the stiffness according to equation (2.4). A vibration isolation system with an extremely large mass is not practical in its use, so the low eigenfrequency should be achieved by lowering the stiffness. Designing a mechanical system that can carry a significant load with little stiffness and damping is an interesting mechatronic challenge, where permanent magnets definitely have its use.

Transmissibility

Transmissibility was defined earlier as the ratio between the displacement of the floor and the displacement of the mass, but could also have been defined as the ratio between the velocity or acceleration of the floor and mass. From

$$x_m = T x_f$$

we can derive that the relation between the floor by taking the derivative to time

$$\frac{dx_m}{dt} = \frac{dT}{dt} x_f + \frac{dx_f}{dt} T \quad (2.10)$$

When the damping and stiffness of the system do not change over time, the first term of equation (2.10) becomes zero and we find that the ratio between \dot{x}_m and \dot{x}_f is again the same transmissibility T :

$$\frac{\dot{x}_m}{\dot{x}_f} = T \quad (2.11)$$

The same procedure holds for the acceleration. When equation (2.10) is differentiated to the time, we find that

$$\frac{\ddot{x}_m}{\ddot{x}_f} = T \quad (2.12)$$

This information is very useful because it means that the transmissibility of a system can be measured using a displacement sensor like a laser, a velocity sensor like a geophone, or an acceleration sensor like an accelerometer.

2.3 Commercial vibration isolation systems and their performance

There are multiple ways to create a support that has a low stiffness. Most commercial systems use pneumatics, active control, or a combination of mechanical springs to do this. The working principle of these three methods will be discussed below, as well as their performance.

Passive pneumatic vibration isolation system

Pneumatic vibration isolation systems, also referred to as airpots, make use of a number of pressure cylinders which support a heavy mass. A schematic overview of such a cylinder is shown in figure 2.4. In this image we see a piston, a pressurized volume and a diaphragm. The diaphragm is an air-tight seal and keeps the volume pressurized, while allowing the piston to move up and down. The pressure causes a load bearing capacity equal to

$$F = p A_{piston}$$

where p is the pressure in the volume and A_{piston} the area of the piston. The pressure is kept constant by an air supply, creating a system with a low stiffness.

Table 2.1: A comparison of the performance of a number of commercially available vibration isolation systems. The performance data is obtained from the manufacturers websites. The advantage of active systems is that they have no eigenfrequency peak f_n . The minus k BM-8 is the overall best performing system found.

Brand	Type	f_n [Hz]	Transmissibility		Load [kg]	Principle
			1 Hz	10 Hz		
minus k	BM-6	2.5	1	0.2	4.5 – 48	combining stiffness
minus k	BM-8	0.5	0.2	0.005	4.5 – 115	combining stiffness
table stable	AVI-400	-	0.84	0.02	0 – 400	active
nanosurf	isostage	-	0.85	0.016	0 – 8	active
Thorlabs	PTP602	4.5	1	0.27	275 – 1100	passive pneumatic
Newport	Integrity 2VCS	1.5	1	0.03	0 – 114	passive pneumatic
Kinetic systems	2200	2.1	1	0.09	0 – 91	passive pneumatic

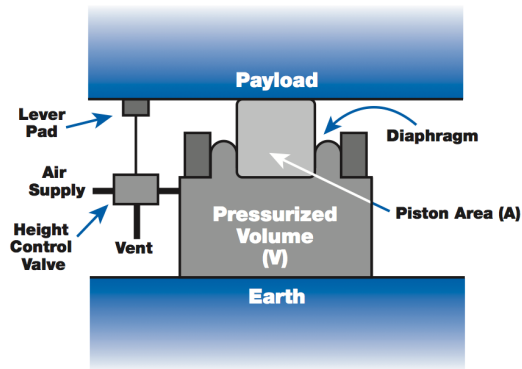


Figure 2.4: Working principle of a pneumatic vibration isolation system. The payload is supported by a piston that moves in a pressurized volume, create a low stiffness system. Obtained from [1]

In reality, pneumatic vibration isolation systems have eigenfrequencies between the 1 Hz and 4.5 Hz, depending upon the brand and price range as is shown in table 2.1. The stiffness in a pneumatic vibration isolation system is caused by a combination of the stiffness of the diaphragm and the consistency of the pressure in the volume. Known producers of pneumatic vibration isolation tables are Newport, TMC, Thorlabs and Kinetic systems.

Mechanical vibration isolation systems

MinusK is a brand that creates mechanical vibration isolation systems by combining springs with a positive and negative stiffness. A schematic drawing of their system is shown in figure 2.5a. If we only focus on the vertical vibrations, the system can be simplified to a load bearing spring and two buckling beams, as shown in figure 2.5b. A support spring with a high load bearing capacity but low stiffness is used to carry the weight, while two negative-stiffness flexures—e.g. buckling beams—are used to compensate for this stiffness. The MinusK vibration isolation systems are one of the best performing on the market and have eigenfrequencies between 0.5 Hz and 2.5 Hz as is shown in table 2.1.

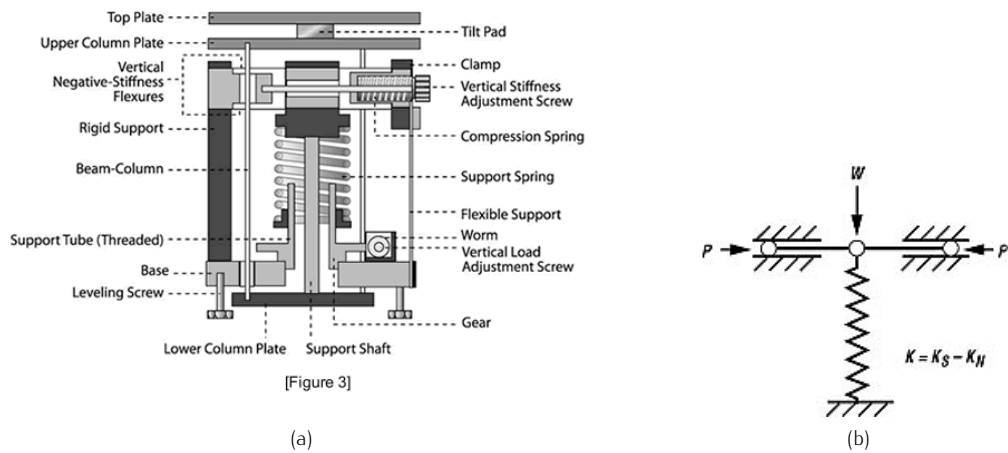


Figure 2.5: (a) Schematic drawing of a minus k system. Because this thesis is focused on vertical vibrations only, we can simplify the system, as is shown in (b). The stiffness of the load carrying spring is compensated for by two buckling beams with a negative stiffness. Obtained from [10].

Active vibration isolation systems

Active vibration isolation systems, like the systems from *Table Stable*, make use of actuators, sensors and feedback control to create a low stiffness. An advantage of these systems is that the controller can compensate for the large gain present at the eigenfrequencies of the system. However the active components used to control the system introduce noise into the system. Literature reports that this electronics-noise can become the limiting factor when active vibration isolation systems are used in an environment with little vibrations [3]. One option to reduce this noise is to improve the electrical component, a task outside the field of mechanical engineering. A second option is to completely exclude to noise by removing the needs for active control: e.g. creating a passive system.

2.4 The passive magnetic vertical vibration isolation system

There is something “right” about the design philosophy of the passive mechanical vibration isolation systems. Table 2.1 on the preceding page shows that—at the moment of writing—the Minus K BM-8 has the best performance of all high-end systems from different manufacturers. There are many more models from Minus K that have a performance similar to the performance of the BM-8 [10].

The design philosophy behind the passive magnetic vibration isolation system is to create a system similar to a Minus K system, but replace the mechanical support spring (see figure 2.5) by a magnetic spring k_m , also referred to as the ‘gravity compensator’. The hypothesis is that combining a high-force, low-stiffness magnetic spring with a low-force, low-stiffness mechanical spring might result in a system with a very low sub-hertz eigenfrequency. Figure 2.6 shows how this system will look like on a system design level. The vibration isolated mass m_1 is supported by the magnetic gravity compensator k_m , while a mechanical linear guide with stiffness k_s and damping c_s is used to stabilize the gravity compensator (see section 4.4 on page 38). A intermediate body m_2 is used to ‘pre-tension’ the magnetic spring, and the position z_2 of the intermediate body is imposed by means of a stiff mechanism.

Advantages of a passive magnetic vibration isolation system are: that there are magnetic configurations that can carry a load with very low stiffness (see chapter 4 on page 29); that

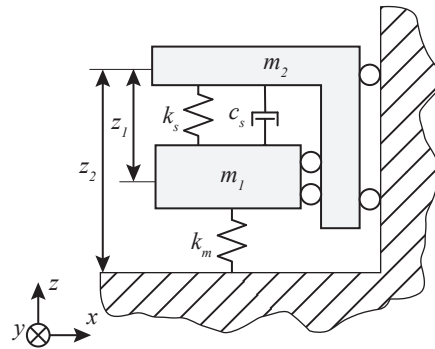


Figure 2.6: A schematic drawing of the passive magnetic vertical vibration isolation system, implementing the magnetic gravity compensator k_m , e.g. the magnetic spring. The isolated mass m_1 is suspended by the gravity compensator k_m , and a linear guide with stiffness k_s and damping c_s is used to stabilize the system. An intermediate body m_2 is used to 'pre-tension' the gravity compensator, and the position z_2 of the intermediate body is imposed by means of a stiff mechanism.

magnetic solutions can be relatively compact compared to mechanical solutions; and that, because there is no mechanical contact, there is also no mechanical damping nor mechanical hysteresis in a magnetic system. Creating a passive system has never been attempted in the past, as far is known to the author.

2.5 Amplitude of vibrations in different environments

Section 2.1 explained that the maximum achievable position accuracy of a system is a function of the amplitude and frequency of floor vibrations. The maximum allowable vibrations in certain environments are prescribed by the ISO and VC standards and are shown in figure 2.7.

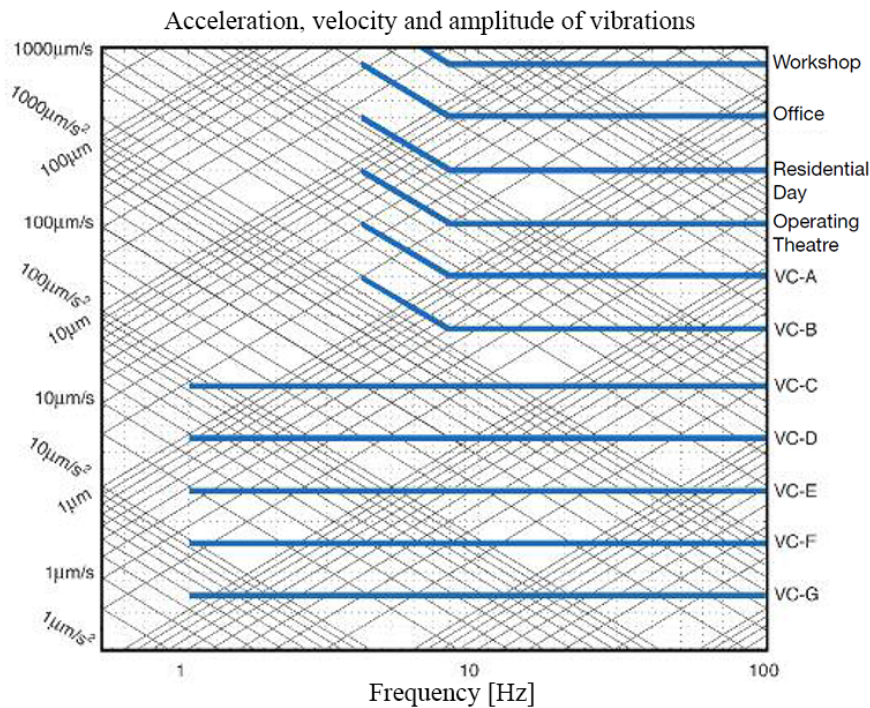


Figure 2.7: The acceleration, velocity and amplitude of vibrations is different environments. Vibrations levels in the workshop, office, residential area and operating theater are ISO standards, while the VC-A to VC-G refer to accepted standards for vibration sensitive tools. Reproduced from [1]

The standards of figure 2.7 make it possible to design vibration sensitive devices for a certain

environment. To return to the example of the microscope: only microscopes with a magnification up to 40x are suitable for use in a normal residential area, when no form of vibration isolation is used [1]. When a vibration isolation system is used, its range should be larger than the amplitude of vibrations. The Mechatronic Systems Design labs at the Delft University of Technology can be classified as office space, meaning that the to-be-designed passive vibration isolation system should have a range of at least $100\mu\text{m}$.

2.6 Conclusions

Vibrations reduce the position accuracy between components of—high tech—devices, because these components are connected with finite stiffnesses. When a high position accuracy is required in a vibration rich environment, a system needs to become very stiff, or needs to be placed upon a vibration isolation system. The performance of such a vibration isolation system is analyzed by measuring the transmissibility of the system. This can be done with both a displacement, velocity, or acceleration sensor. In order to achieve the lowest transmissibility—e.g. the best vibration isolation performance—a passive vibration isolation system should have a low eigenfrequency and contain little damping. The passive magnetic vibration isolation system will support its load using a passive magnetic gravity compensator, which is a magnetic spring with a low stiffness. The Mechatronic Systems Design labs at the Delft University of Technology can be classified as office space, resulting in a minimum range of a vibration isolation system of $100\mu\text{m}$.

Magnetism, magnets and magnetic forces

This chapter is meant to be a quick summary of the parts of electromagnetism that are needed to understand the magnetic concepts discussed in chapter 4. The chapter starts with a recap on electrodynamics, followed by a discussion of permanent magnets and magnetic materials. Next, magnetic circuit theory is introduced as well as how it can be used to calculate reluctance forces. The chapter ends with the introduction of the analytical charge and current models used to calculate the fields and force interaction between permanent magnets in air. Both the magnetic circuit theory and the analytical force and field equations are extensively used in chapter 4 and chapter 5.

For a more in-dept review of electromagnetism, I would advice the very well written introduction by Griffiths [11] and the more advanced text [12]. Also, the more application based text written by Fitzgerald, Furlani, and Munnig Schmidt proved to be extremely useful [13, 14, 8], as well the following thesis [5, 15, 3, 4].

3.1 Electromagnetism and magnetostatics

The behavior of electric and magnetic fields is described by the four Maxwell's equations, which can al be written in integral and differential form. Gauss's law tells that the nett charge Q_{enc} contained in a closed surface S is equal to the surface integral of the electric field \mathbf{E} over this same surface [11].

$$\oint_S \mathbf{E} \cdot d\mathbf{a} = \frac{Q_{enc}}{\epsilon_0}, \quad \nabla \cdot \mathbf{E} = \frac{\rho}{\epsilon_0} \quad (3.1)$$

where ϵ_0 is the permittivity of free space and ρ the charge density. There exists a similar—and nameless—equation for magnetic fields that states that the surface integral of the magnetic flux density \mathbf{B} is always zero when integrated over a closed surface S [11].

$$\oint_S \mathbf{B} \cdot d\mathbf{a} = 0, \quad \nabla \cdot \mathbf{B} = 0 \quad (3.2)$$

This means that the number of magnetic field lines entering the closed surface should be equal to the amount of field lines leaving this surface.

The flux density \mathbf{B} and electric field \mathbf{E} are related by Faraday's law, which tells us that a changing flux density piecing a open surface S results in an electric field in the closed contour C surrounding that surface [11].

$$\oint_C \mathbf{E} \cdot d\mathbf{l} = -\frac{d}{dt} \int_S \mathbf{B} \cdot d\mathbf{a}, \quad \nabla \times \mathbf{E} = -\frac{\partial \mathbf{B}}{\partial t} \quad (3.3)$$

While electric fields are created by static charges, magnetic fields are created by moving charges. The relation between a current piercing an open surface S , and the magnetic field created in the contour C enclosing this surface is called amperes law [11].

$$\oint_C \mathbf{B} \cdot d\mathbf{l} = \mu_0 \mathbf{I}_{enc} + \mu_0 \epsilon_0 \frac{d}{dt} \int \mathbf{E} \cdot d\mathbf{a}, \quad \nabla \times \mathbf{B} = \mu_0 \mathbf{J}_{encl} + \mu_0 \epsilon_0 \frac{\partial \mathbf{E}}{\partial t} \quad (3.4)$$

where μ_0 is the permeability of free space, that is equal to $4\pi \cdot 10^{-7}$ N/Am. The total amount of magnetic flux density passing through a certain area S is called the magnetic flux ϕ [11].

$$\phi = \int_S \mathbf{B} \cdot d\mathbf{a} \quad (3.5)$$

The magnetic flux is measured in *weber* (Wb) and is very useful in *magnetic circuit theory*, discussed later this chapter. From Faraday's law we know that a changing magnetic field results in a electric field. The potential difference—or voltage e —in the contour C enclosing the \mathbf{B} -field is equal to the time derivative of the flux times the number of windings N through which the magnetic flux it passes [11]:

$$e = N \frac{d\phi}{dt} \quad (3.6)$$

In engineering text, the number of windings times the flux is often called the flux linkage $\lambda = N\phi$ [13]. The derivative of the flux linkage to the current flowing in the contour C is called the inductance L :

$$L = \frac{d\lambda}{di} \quad (3.7)$$

In many engineering applications, such as motors or magnetic vibration isolation system, the frequencies at which magnetic and electric field change are relatively low¹. When this is the case, we speak about magnetostatics; meaning that we can neglect the time derivative in Amperes law.

Fields in matter

The current that causes magnetic flux density \mathbf{B} is a combination of bound and free current $\mathbf{I}_{enc} = \mathbf{I}_{enc}^{free} + \mathbf{I}_{enc}^{bound}$. We we talk about current in mechanical systems, we talk about the free current, which makes equation (3.4) inconvenient to work with. Therefore, the magnetic field intensity \mathbf{H} —in physics called the axillary field—is introduced [13, 11]. The relation between the \mathbf{B} and \mathbf{H} field is given by

$$\mathbf{B} = \mu \mathbf{H} \quad (3.8)$$

where the permeability $\mu = \mu_0 \mu_r$ is a function for nonlinear materials and else a constant. An other way of calculating the permeability is by introducing the magnetic susceptibility χ_m :

$$\mu = \mu_0 (\chi_m + 1)$$

We can rewrite the all Maxwell equations for fields in matter, but the one most used is Amperes law:

$$\oint_C \mathbf{H} \cdot d\mathbf{l} = \mathbf{I}_{free}^{enc} + \frac{d}{dt} \int_S \mathbf{D} \cdot d\mathbf{a}, \quad \nabla \times \mathbf{H} = \mathbf{J}_{free} + \frac{\partial \mathbf{D}}{\partial t} \quad (3.9)$$

where \mathbf{J}_{free} is the free current density [A/m²].

¹Below the megahertz (Mhz).

3.2 Magnetic dipole moment and magnetization

Magnetic fields are always the result of moving charges. In the case of a coil, these moving charges are in the form of a macroscopic current \mathbf{I} . Permanent magnets—such as the neodymium magnets used in this research—have no macroscopic current flowing through them. Here, the magnetic field is caused by a microscopic current loop, as shown in figure 3.1b. The area enclosed by the loop times the current is called the *magnetic dipole moment* \mathbf{m} [Am^2][11]

$$\mathbf{m} = I \int d\mathbf{a}$$

which is the ‘source’ of magnetism in permanent magnets. The model of visualizing a magnetic dipole as a microscopic current loop is referred to as the Amperian or current model and is—as far as engineering concerns—physically correct. A different model is the Gilbert, Coulomb or charge model, which visualizes a magnetic dipole as a combination of a positive and a negative ‘magnetic charge’, as shown in 3.1a. Although magnetic monopoles have never been found nor created until now, both methods can be used for calculations and give equivalent results [3].

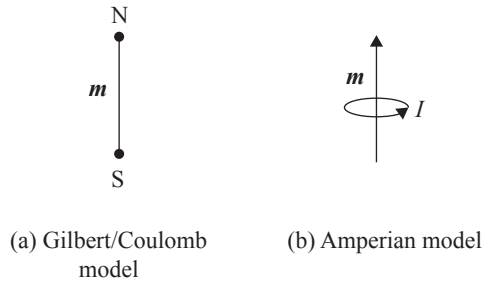


Figure 3.1: The (a) Gilbert or Coulomb model and (b) Amperian model to describe the magnetic dipole moment \mathbf{m} . Partly reproduced from [11].

When simulating magnetic fields—analytically or with FEM software like COMSOL—you need to know the magnetic dipole moment per unit volume, which is called the magnetization \mathbf{M} [14]:

$$\mathbf{M} = \lim_{\Delta V \rightarrow 0} \frac{\sum_i \mathbf{m}_i}{\Delta V} \quad (3.10)$$

and is measured in ampere per meter (A/m). From equation (3.10) we can see that a material can only have a magnetization \mathbf{M} when the magnetic dipoles \mathbf{m}_i are aligned, otherwise the vectors would add up to zero. The magnetization adds to the \mathbf{H} field according to the constitutive relation [14]:

$$\mathbf{B} = \mu_0(\mathbf{H} + \mathbf{M}) \quad (3.11)$$

From equation 3.11 we can deduce that the \mathbf{H} field is discontinuous at the edge of a magnet, and is lower outside the magnet, while the \mathbf{B} field is continuous. This is an easy way to check COMSOL simulations for errors or forgotten magnetizations.

3.3 Permanent magnets and magnetic materials

Most magnetic materials can be classified as paramagnetic, diamagnetic or ferromagnetic materials. All three types of materials behave different in magnetic fields, so it is important to know the difference when designing a magnetic gravity compensator.

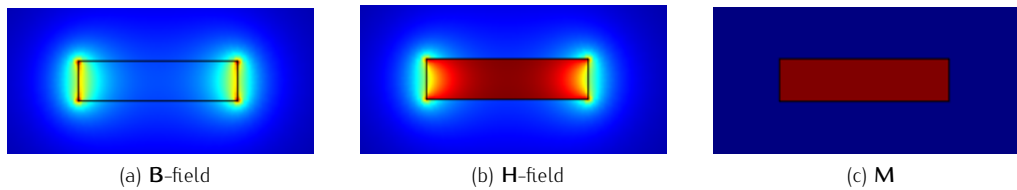


Figure 3.2: The (a) **B**-field, (b) **H** field and (c) magnetization of the same rectangular magnet, simulated with a 2D mfc COMSOL simulation. The colorbal goes from red (high) to blue (low).

Paramagnetic materials are materials which acquire a magnetization parallel to the magnetic field in which they are placed. These materials have a small positive magnetic susceptibility χ_m and thus a relative permeability μ_r larger—but close to—one. Therefore, paramagnetic materials are slightly attracted to magnetic field, but they do not retain there magnetization when the external field is removed. A well known paramagnetic material is aluminum, but also stainless steel can be paramagnetic, as is shown in table 3.1.

Diamagnetic materials are materials which acquire a magnetization opposing the external magnetic field. They have a negative magnetic susceptibility χ_m and a relative permeability $\mu_r < 1$, meaning they are repulsed by magnetic fields. A magnetic field prefers to move around diamagnetic materials. Superconductors can be seen as perfect diamagnetic materials; as they have a relative permeability of zero, no field lines will move through the surface. Bismuth is one of the stronger diamagnetic materials (table 3.1).

Ferromagnetic materials are materials which acquire a magnetization parallel to the external field, just like paramagnetic materials. However, for ferromagnetic materials the magnetic dipoles \mathbf{m}_i align much better, resulting in a large positive magnetic susceptibility χ_m and a high relative permeability. This means that ferromagnetic materials are strongly attracted to magnetic fields. When the external field is removed, ferromagnetic materials can maintain their magnetization, in which case they are called magnetized. As the name suggests, iron is a ferromagnetic material (table 3.1).

Table 3.1: A list of magnetic materials, with their class and relative permeability. A $\mu_r > 1$ indicates that the material is attracted to magnetic fields. Values obtained from [en.wikipedia.org/wiki/Permeability_\(electromagnetism\)](http://en.wikipedia.org/wiki/Permeability_(electromagnetism))

Material	Relative permeability μ_r	Class
Iron (99.95 % pure)	200000	Ferromagnetic
Iron (99.8% pure)	5000	Ferromagnetic
Stainless steel (Ferritic)	1000-1800	Ferromagnetic
Stainless steel (Austenitic)	1.003-7	Paramagnetic
Aluminum	1.000022	Paramagnetic
Bismuth	0.999834	Diamagnetic
Superconductors	0	Diamagnetic (perfect)

When literature refers to magnetic materials, they often mean ferromagnetic materials. These ferromagnetic materials can be further subdivided in soft magnetic materials and hard magnetic materials, e.g. permanent magnets. The difference between soft and hard magnetic materials has to do with intrinsic coercivity, which is explained in the next section.

The hysteresis loop and coercivity

When a ferromagnetic material is placed in an external field \mathbf{H} , its magnetic dipoles align with the field (figure 3.3a). But after the \mathbf{H} field is removed, the magnetic dipoles do not completely move back to their original orientation and a certain amount of magnetization \mathbf{M} remains (see figure 3.3a). This can be imagined as a friction effect according to [8]. Ferromagnetic materials show a certain amount of hysteresis because of this ‘friction’. This hysteresis is unwanted in a gravity compensator because it causes energy loss and will show as damping.

The relation between the magnetization \mathbf{M} and the externally applied field \mathbf{H} is given by a curve called the *intrinsic curve*, shown in red in figure 3.3. We can also draw this curve for the $\mathbf{B} - \mathbf{H}$ relation, called the *normal curve*, which is more common in engineering oriented texts.

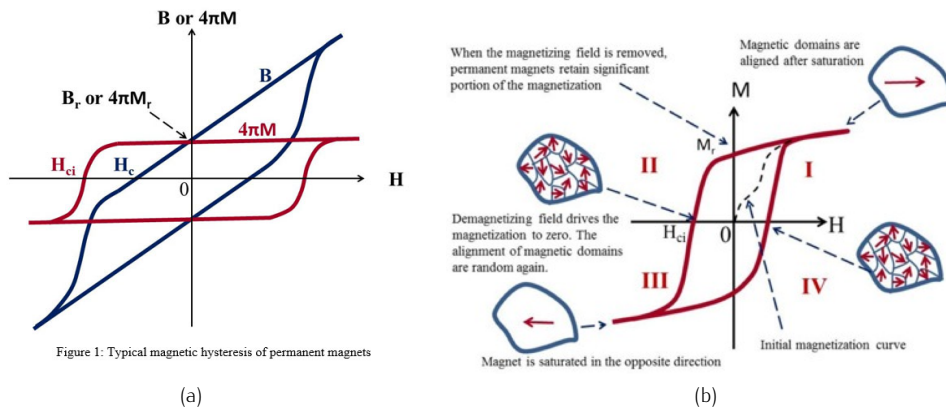


Figure 3.3: The normal curve (blue) and intrinsic curve (red) of a ferromagnetic material

There are four important points marked in figure 3.3a, namely: the remanent flux density \mathbf{B}_r , the remanent magnetization \mathbf{M}_r , the coercivity \mathbf{H}_c and the intrinsic coercivity \mathbf{H}_{ci} . The Remanent flux density (\mathbf{B}_r) is the flux density that remains in the material when the external \mathbf{H} -field is reduced to zero. The relation between the magnetic flux density and the remanent flux density is given by:

$$\mathbf{B} = \mu_0 \mu_r \mathbf{H} + \mathbf{B}_r \quad (3.12)$$

The remanent flux density is a very useful variable, and it the standard of magnet suppliers to define the strength of their magnets. COMSOL allows the use of both \mathbf{B}_r and \mathbf{M}_r . The remanent magnetization (\mathbf{M}_r) is the magnetization that remains in the material when the external \mathbf{H} -field is reduced to zero. The coercivity (\mathbf{H}_c or \mathbf{H}_{cb}) is the \mathbf{H} -field required to reduce the flux density to zero, while the intrinsic coercivity (\mathbf{H}_{ci} or \mathbf{H}_{cj}) the \mathbf{H} -field required to reduce the magnetization to zero.

The intrinsic coercivity represents the magnets its ability the resist demagnetization. When a magnetic material has a low intrinsic coercivity, it is called a soft magnetic material. These materials are not useful as magnets, as external fields will demagnetize the material. Hard magnetic materials are used as permanent magnets, and have a far higher intrinsic coercivity of up to 1500 kA/m.

3.4 Magnetic forces

Within magnetostatics there are two forces: the reluctance force and the lorentz force. The reluctance force is a force between a magnet and a ferromagnetic material—like iron—and

is caused by a change in reluctance \mathcal{R} . The Lorentz force is a force acting on a current—or permanent magnet—in a magnetic field. An easy way to identify if a force is a reluctance or a Lorentz force, is to see if the force can become repulsive. A repulsive force can never be a reluctance force and thus must be a Lorentz force². The differences between reluctance and Lorentz forces are summarized in table 3.2. Both forces can be used to create a low stiffness gravity compensator, but more on that in chapter 4.

Table 3.2: Overview of the differences between reluctance and Lorentz forces. Adapted from [16]

	Reluctance force	Lorentz force
Basic computation principle	energy in magnetic field	cross-product of current and flux density
Computation formula	$\mathbf{F} = \frac{\partial W}{\partial \mathbf{x}}$	$\mathbf{F} = \mathbf{i} \times \mathbf{B}$
Direction of force	perpendicular to the surface of materials of different μ_r	Perpendicular to flux density
Attractive/repulsive	always attractive	attractive or repulsive
Example	magnet sticking on a fridge	DC-motor, interaction between permanent magnets, speaker

3.5 Calculating forces in systems with a well defined flux path

Magnetic circuit theory

Most magnetic circuits, such as actuators, transformers, and a number of gravity compensators, have a well defined magnetic flux path. They use materials with a high relative permeability, through which nearly all magnetic flux ϕ travels. The idea of magnetic circuit theory is that, because of this well defined flux path, we can simplify the three dimensional magnetic system to a one dimensional one.

Magnetic circuit theory is extremely similar to electric circuit theory: we have a source of magnetism called the magnetomotive force \mathcal{F} , a magnetic resistance called the reluctance \mathcal{R} , and the magnetic current which is the magnetic flux ϕ [8, 17]. The cause of the magnetomotive force can be a coil (figure 3.4a) or a magnet (figure 3.4b). The highly reluctant material of figure 3.4ab is modeled as wires in figure 3.4, and airgaps become reluctances.

In case there is a coil, the magnetomotive force follows from 3.9 [13]:

$$\mathcal{F} = \oint_C \mathbf{H} \cdot d\mathbf{l} = Ni \quad (3.13)$$

where N is the amount of turns and i is the real current flowing through the coils. Because the length of the flux path C is equal to the length of the core plus the length of the airgap, 3.13 becomes:

$$\mathcal{F} = H_c l_c + H_g g \quad (3.14)$$

Using equations 3.8, 3.5, 3.2, the above can be rewritten as:

²You could classify forces on diamagnetic materials like bismuth as reluctance forces. In so then reluctance forces can become repulsive. However, these forces are extremely small and not useful for engineering applications.

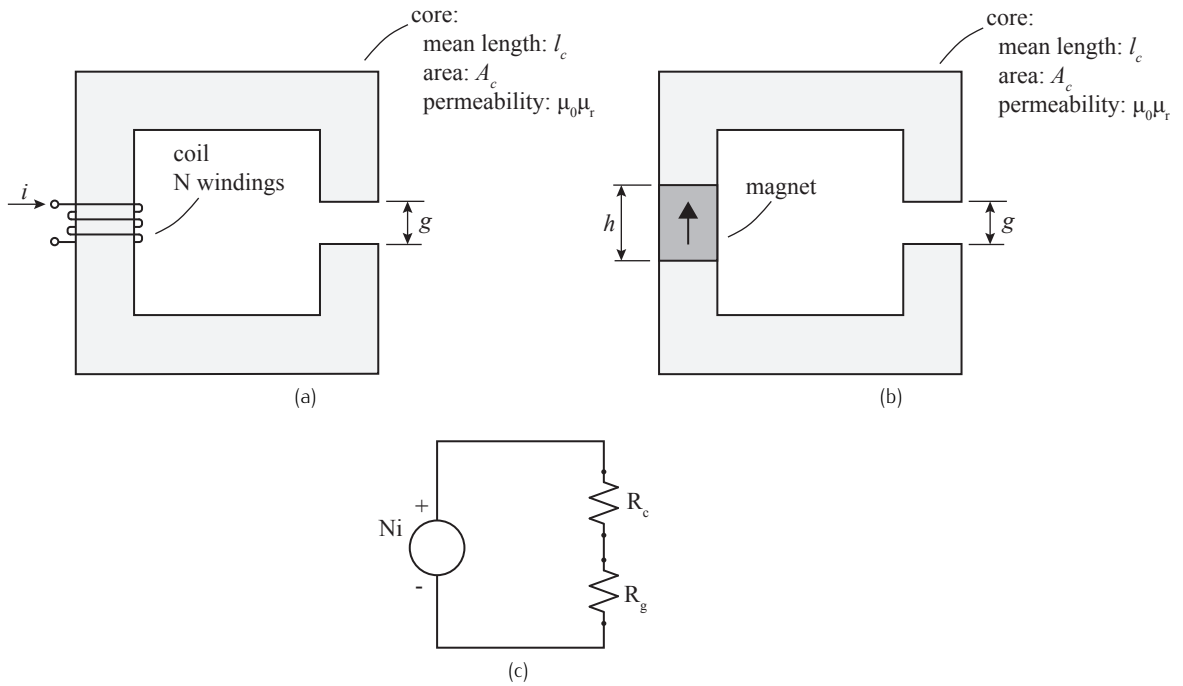


Figure 3.4: Magnetic circuit theory. (a) shows a three dimensional magnetic circuit with a coil as source, while in (b) the magnetomotive force \mathcal{F} is caused by a permanent magnet. The magnetic circuit representation of (a) is shown in (c).

$$\mathcal{F} = \phi \left(\frac{l_c}{\mu A_c} + \frac{g}{\mu_0 A_g} \right) \quad (3.15)$$

which hints that the terms between the brackets are the reluctances, so that

$$\mathcal{F} = \phi(\mathcal{R}_c + \mathcal{R}_g) \quad (3.16)$$

When the magnetic circuit does not only contain coils but also permanent magnets, we can still determine the magnetomotive force \mathcal{F} and all above is still valid. A permanent magnet can be modeled as a fictitious coil where the current times the number of windings is equal to the magnetic field strength times the length of the magnet [13]:

$$(Ni)_{equiv} = -H_c h \quad (3.17)$$

From equation (3.2) follows that all magnetic flux that travels through the core should go into the airgap and its surroundings. So it must be true that the field in the gap is equal to

$$B_g = \frac{\gamma\phi}{A_g} \quad (3.18)$$

where γ is a loss factor to take stray flux into account. Now the field is known, we can calculate the forces. In case of a Lorentz force can use the Lorentz equation (equation (3.26)), while reluctance forces follow from the energy balance.

The energy balance

Energy cannot be created nor destroyed. Therefore we can write down an energy balance for systems with an electromechanical energy conversion, like the system shown in figure 3.5.

$$\left(\begin{array}{c} \text{Energy input} \\ \text{from electric} \\ \text{sources} \end{array} \right) = \left(\begin{array}{c} \text{Mechanical} \\ \text{energy} \\ \text{output} \end{array} \right) + \left(\begin{array}{c} \text{Increase in energy} \\ \text{stored in magnetic} \\ \text{field} \end{array} \right) + \left(\begin{array}{c} \text{Energy} \\ \text{converted} \\ \text{into heat} \end{array} \right) \quad (3.19)$$

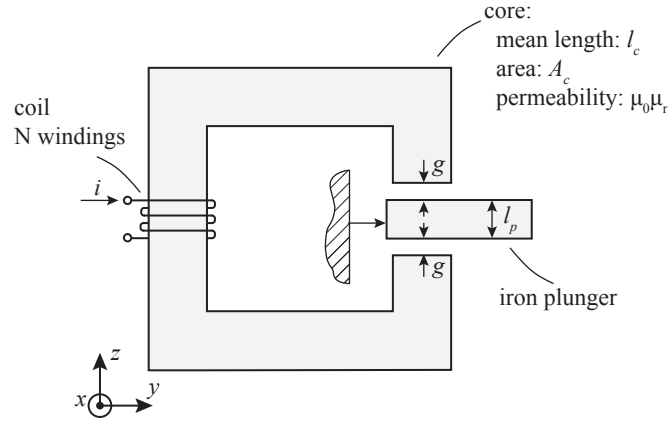


Figure 3.5: A system with an electromechanical energy conversion. Conform with equation (3.17), the coil can also be seen as a permanent magnet.

The energy balance states that the mechanical output of a electromechanical system must be equal to the electrical energy input, minus the losses and the decrease in energy stored in the magnetic field. If we take the losses out of our system and take the time derivative of the energy balance, we get the power balance:

$$\frac{dW_{fld}}{dt} = \underbrace{ei}_{\dot{W}_{elec}} - \underbrace{F_{fld} \frac{dx}{dt}}_{\dot{W}_{mech}} \quad (3.20)$$

where F_{fld} is the force caused by the magnetic field. Substitution of equation (3.6) in equation (3.20) results in the following energy balance:

$$dW_{fld} = id\lambda - F_{fld}dx \quad (3.21)$$

Since the system is lossless, the magnetic field energy is fully defined by the two state variables λ and x . So it must be true that:

$$dW_{fld}(\lambda, x) = \left. \frac{\partial W_{fld}}{\partial \lambda} \right|_x d\lambda + \left. \frac{\partial W_{fld}}{\partial x} \right|_\lambda dx \quad (3.22)$$

By comparing equation (3.21) and equation (3.22) we see that it must be true that the reluctance force is negative proportional to the derivative of the field energy, while keeping the flux linkage constant [13]:

$$F_{fld} = - \left. \frac{\partial W_{fld}(\lambda, x)}{\partial x} \right|_\lambda \quad (3.23)$$

The subscript right of the partial derivatives indicate that the derivative should be taken with the variable constant. This is a mathematical trick and does not mean that λ or x should be constant during operating the device.

When analytically solving equation (3.23) is troublesome, the coenergy of the field W'_{fld} can be used in stead of the energy W_{fld} . The coenergy is defined as [13]:

$$W'_{fld}(i, x) = i\lambda - W_{fld}(\lambda, x) \quad (3.24)$$

and gives the exact same results for the reluctance force, when the below formula is used:

$$F_{fld} = - \left. \frac{\partial W'_{fld}(\lambda, x)}{\partial x} \right|_i \quad (3.25)$$

The only difference it that now the current is kept constant during differentiation.

Because the goal of this research is to create a passive system, all magnetic concepts discussed in chapter 4 use permanent magnets instead of coils. However, equation (3.23) and equation (3.25) are still applicable if we apply equation (3.17) and replace the magnets by fictions coils in the calculation.

The Lorentz equation

The Lorentz force is the force acting on a charge q as result of an electromagnetic field and is equal to:

$$\mathbf{F}_l = q(\mathbf{E} + \mathbf{v} \times \mathbf{B}) \quad (3.26)$$

In the absence of an electric field, the Lorentz force becomes:

$$\mathbf{F}_l = \mathbf{I} \times \mathbf{B} \quad (3.27)$$

In section §3.2 we talked about the magnetic dipole \mathbf{m} and how it could be modeled as two magnetic charges or as a small current loop. And if we would place this dipole—or small current loop—in a magnetic field, one would expect a Lorentz force acting on the dipole. This is indeed the case, and the Lorentz force acting on the magnetic dipole is equal to [11]:

$$\mathbf{F}_l = \nabla(\mathbf{m} \cdot \mathbf{B}) \quad (3.28)$$

As permanent magnets consist of large amounts of aligned magnetic dipoles, they can also be modeled as a number of magnetic charges or currents, and also have a Lorentz force acting on them when placed in a magnetic field.

3.6 Calculating forces in systems with a undefined flux path

When the magnetic flux path is well defined by highly permeable materials like iron, magnetic circuit theory can be used to calculate the magnitude of the B-field. When the magnets are located in free space, the flux path becomes three dimensional making magnetic circuit theory useless. Determining the magnetic field can now be done with a FEM program such as COMSOL, but when magnets have simple geometries it is possible to calculate the magnetic field analytically. The advantage of such a analytical model is that it greatly reduces the required computational power compared to a FEM programs. With this great reduction of computational power, it becomes possible to optimize the size, shape and topology of a magnetic gravity compensator for a certain force-displacement curve.

The field of a permanent magnet can be modeled using the charge model or using the current model. Both models are discussed below and should give identical results [14].

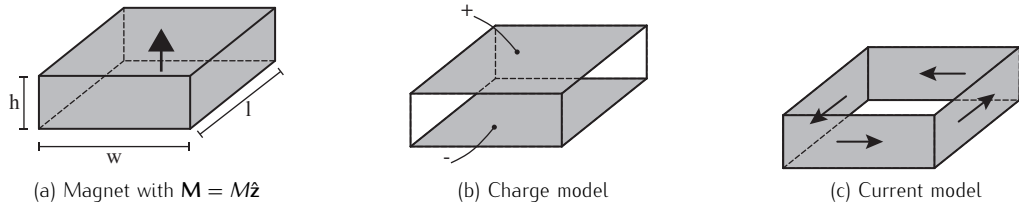


Figure 3.6: This figure shows (a) a permanent magnet with an upwards magnetization modeled as (b) positive and negative charges at the top and bottom of the magnet and as (c) four current sheets.

The charge model

The charge model builds upon the Gilbert model and models permanent magnets as an amount of imaginary positive and negative magnetic charges. These positive and negative charges are located at the top and bottom plates of the magnet, as is shown in figure 3.6.

When a magnet is modeled as magnetic charges there are no currents, so the curl of the H-field is equal to zero $\nabla \times \mathbf{H} = \mathbf{0}$ according to Amperes law. Because the H-field is irrotational, it is allowed to introduce a magnetic scalar potential [14]:

$$\mathbf{H} = -\nabla\varphi_m \quad (3.29)$$

We do not know \mathbf{H} , but we do know the magnetization \mathbf{M} which is a real value within the magnet and zero everywhere else. Substitution of equation (3.11) and $\nabla \cdot \mathbf{B} = 0$ in equation (3.29) results in the solvable relation:

$$\nabla^2\varphi_m = \nabla \cdot \mathbf{M} \quad (3.30)$$

The solution of equation is equal to [14]:

$$\varphi_m(\mathbf{x}) = -\frac{1}{4\pi} \int_V \frac{\nabla' \cdot \mathbf{M}(\mathbf{x}')}{|\mathbf{x} - \mathbf{x}'|} dV + \frac{1}{4\pi} \oint_S \frac{\mathbf{M}(\mathbf{x}') \cdot \hat{\mathbf{n}}}{|\mathbf{x} - \mathbf{x}'|} dS \quad (3.31)$$

and consists of integration over the finite volume V bounded by surface S . The vector \mathbf{x}' points to the source points, while \mathbf{x} points to the observation points. equation (3.31) is found using Green's functions, a mathematical trick very well described in [18, 19, 20, 14]. Finally we can introduce the volume charge density and surface charge density corresponding to the volume and surface integrals:

$$\begin{aligned} \rho_m &= -\nabla \cdot \mathbf{M} \quad \text{volume charge density (A/m}^2\text{)} \\ \sigma_m &= \mathbf{M} \cdot \hat{\mathbf{n}} \quad \text{surface charge density (A/m)} \end{aligned} \quad (3.32)$$

and rewrite equation (3.31) for vacuum $\mathbf{B} = \mu_0\mathbf{H}$ as:

$$\mathbf{B}(\mathbf{x}) = -\frac{\mu_0}{4\pi} \int_V \frac{\rho_m(\mathbf{x}')(\mathbf{x} - \mathbf{x}')}{|\mathbf{x} - \mathbf{x}'|^3} dV + \frac{\mu_0}{4\pi} \oint_S \frac{\sigma_m(\mathbf{x}')(\mathbf{x} - \mathbf{x}')}{|\mathbf{x} - \mathbf{x}'|^3} dS \quad (3.33)$$

The above equation gives the B-field at observation point \mathbf{x} as function of volume and surface charges located at \mathbf{x}' . For normal magnets, the volume charge density is zero ($\rho_m = 0$).

The current model

The current model builds upon the Amperian model and models permanent magnets as a number of current sheets, as is shown in figure 3.6. According to Ampere’s law $\nabla \times \mathbf{H} = \mathbf{J}$. Because the H-field and B-field have a non-zero curl, it is not possible to introduce a magnetic scalar potential. But it is possible to introduce a magnetic vector potential A [11]:

$$\mathbf{B} = \nabla \times \mathbf{A} \tag{3.34}$$

Substitution of the vector potential into Amperes law, and using equation (3.11), we can rewrite equation (3.34)to:

$$\nabla^2 \mathbf{A} = -\mu_0(\mathbf{J} + \nabla \times \mathbf{M}) \tag{3.35}$$

The above equation looks a lot like equation (3.30) and solving it requires similar steps. In stead of charge densities, we can now define a volume current density \mathbf{J}_m and a surface current density \mathbf{j}_m

$$\begin{aligned} \mathbf{J}_m &= \nabla \times \mathbf{M} \quad \text{volume current density (A/m}^2\text{)} \\ \mathbf{j}_m &= \mathbf{M} \times \hat{\mathbf{n}} \quad \text{surface current density (A/m)} \end{aligned} \tag{3.36}$$

Again—using a Green’s function—the solution of equation (3.35) has been found to be [14]:

$$\mathbf{A}(\mathbf{x}) = \frac{\mu_0}{4\pi} \int_V \frac{\mathbf{J}_m(\mathbf{x}')}{|\mathbf{x} - \mathbf{x}'|} dV + \frac{\mu_0}{4\pi} \oint_S \frac{\mathbf{j}_m(\mathbf{x}')}{|\mathbf{x} - \mathbf{x}'|} dS \tag{3.37}$$

The B-field is found by substituting the above equation into equation (3.34)and is equal to:

$$\mathbf{B}(\mathbf{x}) = \frac{\mu_0}{4\pi} \int_V \mathbf{J}_m(\mathbf{x}') \times \frac{(\mathbf{x} - \mathbf{x}')}{|\mathbf{x} - \mathbf{x}'|^3} dV + \frac{\mu_0}{4\pi} \oint_S \mathbf{j}_m(\mathbf{x}') \times \frac{(\mathbf{x} - \mathbf{x}')}{|\mathbf{x} - \mathbf{x}'|^3} dS \tag{3.38}$$

A regular permanent magnet does not contain a volume current density, so $\mathbf{J}_m = \mathbf{0}$. The reason for this is that all internal currents ‘cancel’ each other out, as is illustrated in figure 3.7. A mathematical explanation is that if we integrate the curl of a vector \mathbf{v} over an area S , the result is equal to integral of \mathbf{v} over a perimeter C that encloses S :

$$\int_S (\nabla \times \mathbf{v}) \cdot d\mathbf{a} = \oint_C \mathbf{v} \cdot d\mathbf{l} \tag{3.39}$$

The above equation is called stokes theorem [11].

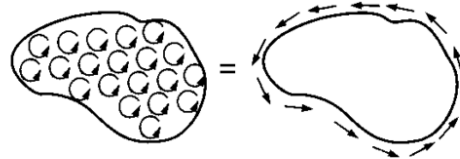


Figure 3.7: In a permanent magnet, all internal current cancel each other out. Only a surface current remains. Image obtained from [11].

1D solution for the field of rectangular magnets

The magnetic flux density B at the centerline of the rectangular magnet of figure 3.6a can be found analytically by solving equation (3.33). This can be done simply by hand because the term $(\mathbf{x} - \mathbf{x}')$ reduces to z because of symmetry and $\mathbf{x} = z\hat{\mathbf{z}}$ and $\mathbf{x}' = x\hat{\mathbf{x}} + y\hat{\mathbf{y}}$. After solving the integrals, the one dimensional equation for B-field in the z -direction becomes:

$$B_z = \frac{B_r}{\pi} \left[\tan^{-1} \left(\frac{(z+h)\sqrt{w^2+l^2+h^2}}{wl} \right) - \tan^{-1} \left(\frac{z\sqrt{w^2+l^2+h^2}}{wl} \right) \right] \quad (3.40)$$

where is used that $B_r = \mu_0 M$ for vacuum and w, h, l are the respective width, height and length of the magnet. Solutions for different shapes of magnets, such as disks, rings and spheres can also be obtained analytically and are found at [21] (without derivation nor reference).

The validity of equation (3.40) is checked by comparing its results with results obtained from a COMSOL mfn³ 3D simulation. As shown in figure 3.8, the results agree well, thus equation (3.40) is most likely a valid representation of the field of a square magnet and therefore can be used to fit the measurement data. The COMSOL simulation results show a strong decrease in flux density for $z > 15$ mm. This is caused by the Infinite Element Domain (IED), used in the simulation to simulate an 'infinitely large' airbox to avoid edge effects, and should be ignored.

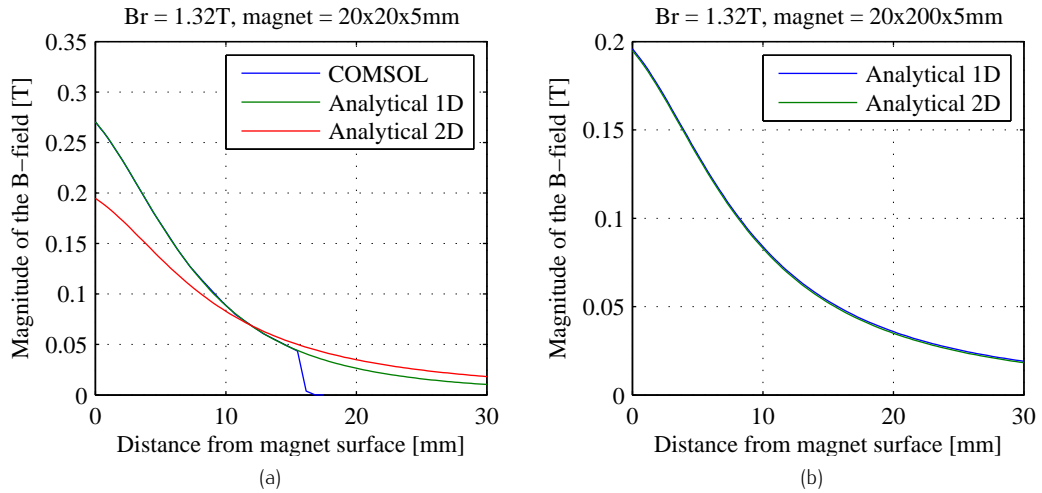


Figure 3.8: The B-field on the centerline of (a) a square permanent magnet and (b) a rectangular magnet with length = 10 x width. For the square magnet, COMSOL results agree with equation (3.40). The sharp decrease in the COMSOL simulation results is caused by the infinite element domain.

2D solution of the field of rectangular magnet

A long rectangular magnet is represented in the current model as two long and two short current sheets. When the length of the magnet is far larger than the width, we can neglect the contribution of the short current sheets to the magnetic field. As result, the solution of equation (3.38) becomes two dimensional and the components of the B-field are given by [14]:

$$B_x(x, y) = \frac{B_r}{4\pi} \left[\ln \left(\frac{(x+w)^2 + (y-h)^2}{(x+w)^2 + (y+h)^2} \right) - \ln \left(\frac{(x-w)^2 + (y-h)^2}{(x-w)^2 + (y+h)^2} \right) \right] \quad (3.41)$$

³A type of COMSOL simulation. mfn stands for: magnetic field no current

and

$$B_y(x, y) = \frac{B_r}{2\pi} \left[\tan^{-1} \left(\frac{2h(x+w)}{(x+w)^2 + y^2 - h^2} \right) - \tan^{-1} \left(\frac{2h(x-w)}{(x-w)^2 + y^2 - h^2} \right) \right] \quad (3.42)$$

and the total B-field is $\mathbf{B} = B_x \hat{\mathbf{x}} + B_y \hat{\mathbf{y}}$. The variables w and h are the width and height of the magnet.

If we only look at the centerline $x = 0$, we can again obtain the one dimensional B-field as function of the distance from the surface. This is not a good idea for square magnets because the field obtained with equations 3.41 and 3.42 will be too low, as is shown in figure 3.8a. The 2D formula's become valid for $L > 10w$ as shown in figure 3.8b.

We can conclude that two dimensional models—analytical or FEM—are not suitable for simulating the field of a square magnet.

3D solution of the field of a rectangular magnet

An analytic equation of the three dimensional field of a rectangular magnet does exist and can be found in [14, 3]. However, implementing and using these equations became such a devious task that it was decided to use COMSOL for all three dimensional simulations.

Force interaction between magnets

When two magnets are placed next to each other and the field created by the first is known, the forces acting on the second magnet can be derived from the Lorentz equation or using the Maxwell stress tensor [14]. Although COMSOL is used for all three dimensional problems in this research. However, some of the concepts of chapter 4 can be simplified. When the magnets are chosen cylindrical of shape and their central axis are aligned, the problem of calculating the forces reduces to a 1D problem. According to [22] the force between thin cylindrical magnets can be approximated with:

$$F_z \approx -\frac{\pi\mu_0 M^2 R^4}{4} \left[\frac{1}{z^2} + \frac{1}{(z+2h)^2} - \frac{2}{(z+h)^2} \right] \quad (3.43)$$

where R and h are the radius and height of the magnets respectively. A "more than satisfactory agreement" between equation (3.43) and measurement data is reported in [22], but is not validated by means of FEM simulations in this thesis.

3.7 Conclusion

Magnetism is created by the alignment of all magnetic dipoles within a material. Magnetizing and demagnetizing a ferromagnetic material results in energy loss because of 'friction between these magnetic dipoles. There are two types of magnetic forces: reluctance forces and Lorentz forces. The procedure for calculating or predicting these forces depends upon how well the flux path is defined. Magnetic circuit theory is only useful for circuits with a well defined flux path, which is often the case in reluctance systems. When airgaps are large, the field can be determined with FEM software such as COMSOL, or—in the absence of iron—with analytical equations. Modeling square magnets in 2D can result in significant errors of more than 20%. Rectangular magnets can only be modeled in 2D when their length is approximately ten times their height.

Part II

Magnetic gravity compensator design and validation

Magnetic gravity compensator concepts

The previous two chapters explained the theory of vibration isolation and magnetic fields and forces. This chapter will combine these theories to evaluate the performance of eight magnetic gravity compensator concepts, with respect to a number of requirements. The concept choice will be defended, and it will be explained how the load bearing capacity and stiffness of the magnetic system could be tuned mechanically. The last two sections of this chapter are dedicated to the stability and robustness to alignment errors of the magnetic gravity compensator concept.

4.1 Requirements of the magnetic system

The magnetic gravity compensator should have a region in which it can support a load with little stiffness and little damping, such that the transmissibility between floor motion x_f and payload motion x_m will be low. Numerous systems have been designed in the past, that used (electro)magnetism to bear a load with low stiffness [2, 3, 4, 5, 6, 7]. However, all those magnetic vibration isolation systems needed some form of active control to keep the system in its low stiffness area. As the goal of this thesis is to create a passive system, no active control can be used to keep the gravity compensator in this region of low stiffness. The magnetic gravity compensator concept should be stable in at least the vertical direction, and that it should be possible to stabilize the concept in all other direction, without adding significant stiffness and damping to the z-direction. The criteria used to evaluate the concepts can be summarized as:

- **Range of the low stiffness region:** The larger the low stiffness region, the easier it will be to position and keep the system in this area.
- **Amount of damping:** The lower the amount of damping, the better the system will isolate vibrations.
- **Stability of the low stiffness area:** Fewer unstable degree's of freedom mean less mechanical constraints needed to keep the system stable.
- **Load bearing capacity:** The higher the load bearing capacity, the lower the eigenfrequency of the system will be, and thus the better it will isolate vibrations.

The ideal force curve of the magnetic gravity compensator is shown in figure 4.1. The red curve shows the upwards force delivered by the system, and the curve has a positive stiffness at both sides of the low stiffness region.

Keeping the gravity compensator in it's low stiffness area is not a problem, when the area is stable. This can be done by mechanical stops.

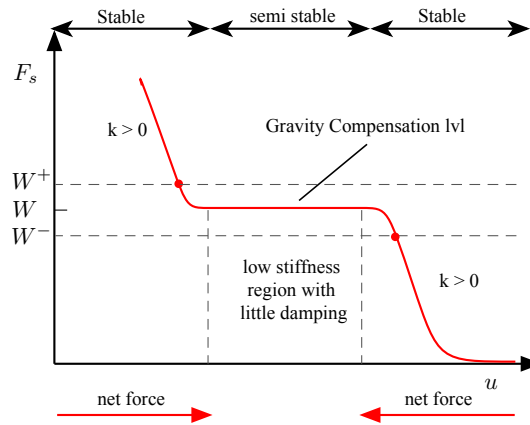


Figure 4.1: The ideal force–displacement curve of the magnetic gravity compensator with a large low stiffness range, enclosed by two positive stiffness ranges.

4.2 Overview and discussion of concepts

There are many magnetic configurations that can be used to create a zero-stiffness region and below the properties of a number of these concepts will be discussed.

The iron mover

A simple way to create a low-stiffness gravity compensator is by moving an iron plunger through a magnetic field created by two permanent magnets, as is illustrated in figure 4.2a. This concept is built and measured by [23], but their work does not physically substantiate the force curve of the concept, reproduced in figure 4.2b. An active system based upon the same magnetic concept is described and validated by [7].

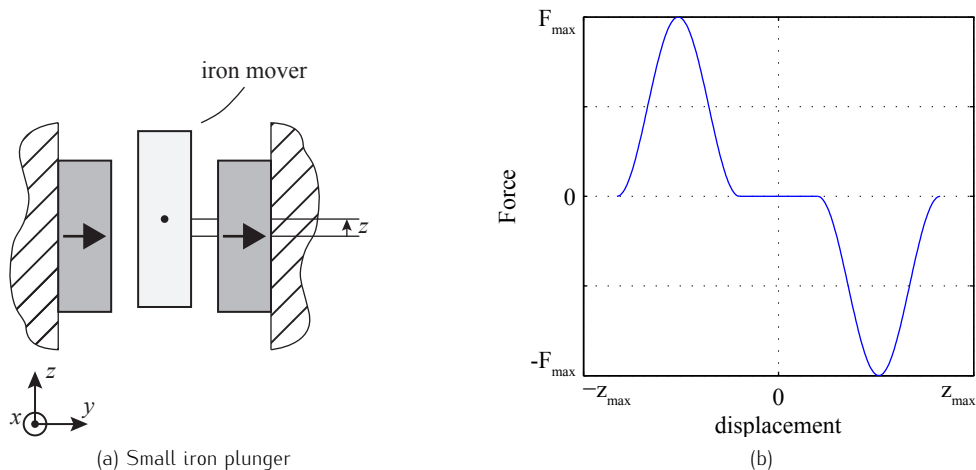


Figure 4.2: The (a) small iron plunger concept and (b) the corresponding force in z -direction acting on the iron plunger. Based upon [23]. The image is not to scale, and the force curve is based upon reasoning.

The force–deflection curve of figure 4.2b shows that the force acting on the iron plunger is such that the plunger always is pulled into the airgap. This agrees with the expectation, as magnets attract iron. When the iron plunger is fully in the airgap—at $z = 0 \pm \delta z$ —the force becomes zero, as there is no more iron to attract. A simplified explanation of the small displacement δz

around $z = 0$, where F_z remains zero is that for $\pm\delta z$ the volume of iron in the airgap does not change. The two regions where there is a force but little stiffness, e.g. the extreme values of figure 4.2b, are suited for use in a gravity compensator.

A more physical way to explain the shape of the force curve is by applying the principle of conservation of energy. As stated in section §3.5, the force acting on a mechanical plunger in a system without losses nor electrical inputs is equal to the partial derivative of the total field energy W_{fld} [13]:

$$F_z = - \left. \frac{\partial W_{fld}(\lambda, z)}{\partial z} \right|_{\lambda} \quad (4.1)$$

Large mover An interesting way to adapt the design shown in figure 4.2a is by increasing the size of the plunger, such that its height is far greater than the size of the magnets, as is shown in figure 4.3a. However this change will not result in a larger low stiffness region suitable for gravity compensation, but rather in a larger distance between the force peaks in the force-plot, as shown in figure 4.3b.

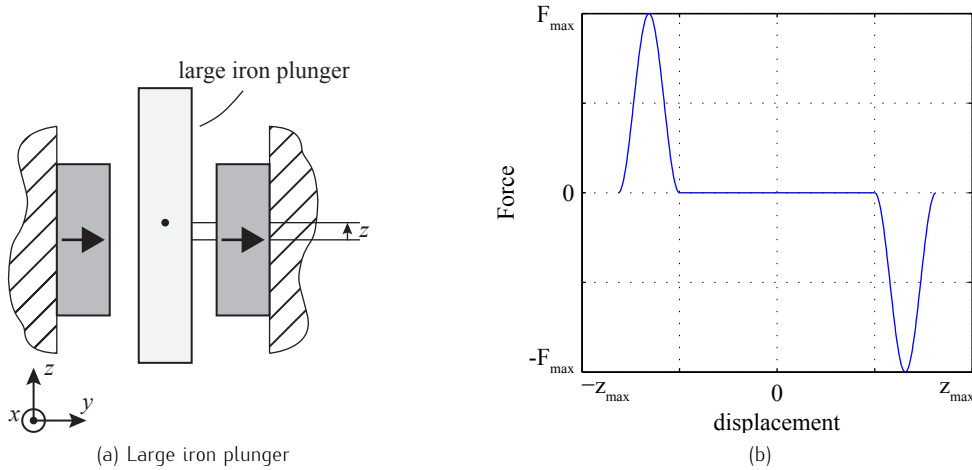


Figure 4.3: The (a) large iron plunger concept and (b) the corresponding force in z -direction acting on the iron plunger. The image is not to scale, and the force curve is based upon reasoning.

The shape of figure 4.3b can be explained with equation (4.1). When the iron moves in the airgap, the energy stored in the airgap reduces, and thus there is a positive force polling the iron in. However, when the airgap is completely filled with iron, there is no further change in W_{fld} and the force reduces to zero. When the length of iron bar increases, the bar can displace more without changing the volume of iron in the airgap, thereby creating a longer range where the force will remain zero.

Adapting field strength and iron shape Increasing the size of the low-stiffness area is thus not done by increasing the length of the iron bar, but rather by shaping the energy stored in the field $W_{fld}(\lambda, z)$. The correct shape of the energy function $W_{fld}(\lambda, z)$ can be found by looking at the second derivative: the stiffness k_z .

The stiffness in z -direction of a mechanism is defined as $k_z = -\partial F_z / \partial z$. Substitution of equation (4.1) results in:

$$k_z = \left. \frac{\partial^2 W_{fld}}{\partial z^2} \right|_{\lambda} \quad (4.2)$$

Therefore, a system with zero stiffness in the z direction needs a field energy W_{fld} that changes linear with z , such that:

$$W_{fld} = \eta z$$

where η is a scalar constant $\forall z$. One possible way of doing this is by shaping the width of the iron plunger. Another way, shown in figure 4.4a, is by using many magnets of different sizes and magnetization \mathbf{M} to create the required field energy function $W_{fld}(z) = \eta z$. Such an energy function should result in the force characteristic shown in figure 4.4b.

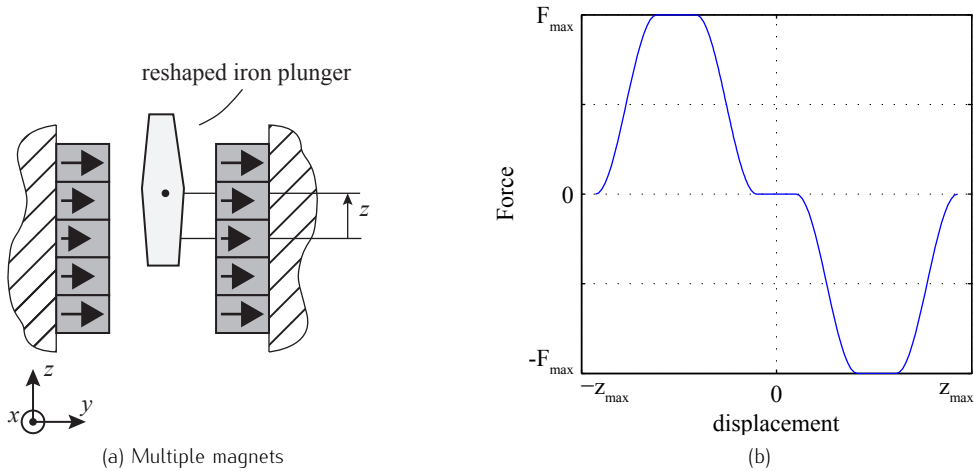


Figure 4.4: The energy stored in the field can be adapted by changing the strength of the magnets and the shape of the iron plunger (a). When both are adapted such that $W_{fld} \propto z$, one would expect a low stiffness region in the force acting on the plunger (b). The image is not to scale, and the force curve is based upon reasoning.

Stray flux Figures 4.2b, 4.3b, and 4.4b show a force and stiffness equal to zero for $z = 0 \pm \delta z$. Although the calculation method is always valid, the plots are only correct in the case that the magnetic field is fully confined in the airgap between the magnets. In reality there will be a certain amount of stray flux, depending upon the dimensions of the gap and the difference in reluctance between the airgap and the iron plunger. Figures 4.2b, 4.3b, and 4.4b are approximations and in reality, the force-displacement curve will never be completely flat around zero.

The Halbach array

A different way to create a gravity compensator is by using a Halbach topology, as shown in figure 4.5a. Six magnetic rings are used to create a magnetic field in which a seventh magnetic ring is allowed to move up and down. The four magnetic rings, located at the top and bottom of the topology, are used to create a high flux density in the airgap, resulting in a high force density [3]. When a high force density is not necessary, these outer magnets can be removed, resulting in the design of figure 4.5b proposed by [5].

The curve describing the force acting on the moving ring as function of z highly depends upon the relative dimensions of the magnets, as shown in figure 4.6 for both topologies. When the height of the static magnets h is equal to the height of the moving magnet, there is a single maximum in the force curve. Increasing h results in a second maximum, whilst reducing the value at both extremes. Both are caused by the phenomena that a magnetic field is far

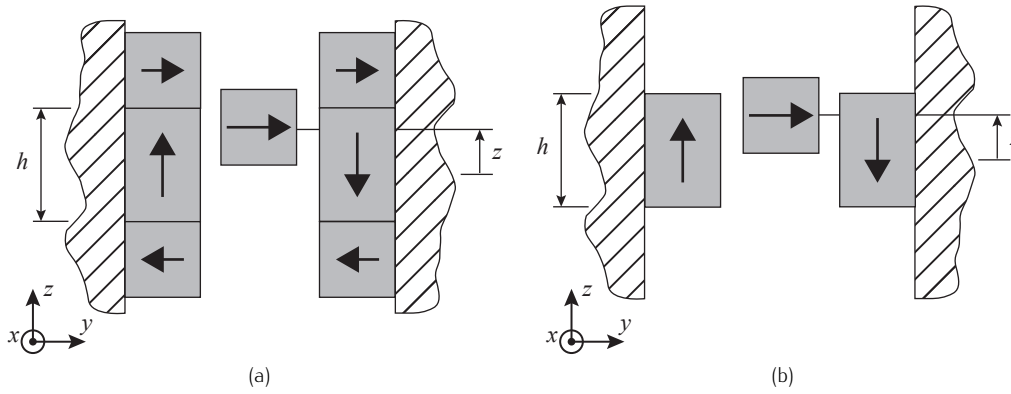


Figure 4.5: A (a) gravity compensator using a quasi-Halbach topology [3] and (b) a simplified version proposed in [5] and [6].

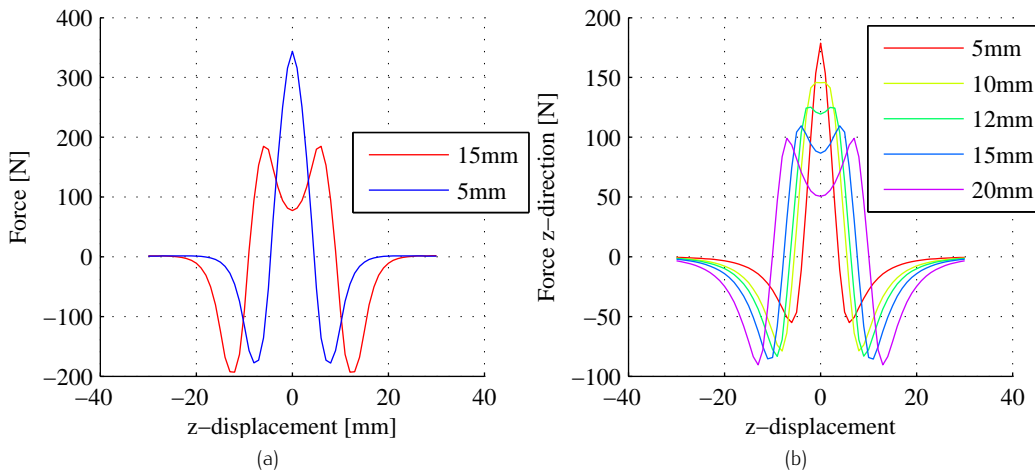


Figure 4.6: Force F_z acting on the moving magnet for the magnetic configuration of (a) figure 4.5a and (b) figure 4.5b. In (a) the flux is concentrated in the air gap, resulting in a significantly higher force for equal magnet volumes. Results obtained with a 2D FEM simulation.

stronger near the edges of the magnet, because at the center of the magnet the dipoles cancel out each other [11]. Analyzing figure 4.6 we see that for both configurations of figure 4.5, there is no h that creates a zero stiffness region larger than a point, thereby rendering the concept unsuitable for a passive magnetic gravity compensator.

Attraction and repulsion

It is also possible to create a gravity compensator with a combination of attractive and repulsive magnets, as shown in 4.7a. When the relative permeability μ_r of the complete volume containing the magnetic field caused by the magnets is equal to one—e.g. there are no soft magnetic materials present—we can apply the principle of superposition for magnetic fields and add the fields \mathbf{B}_{top} and $\mathbf{B}_{\text{bottom}}$ created by the top and bottom magnets so that $\mathbf{B}_{\text{tot}} = \mathbf{B}_{\text{top}} + \mathbf{B}_{\text{bottom}}$. Therefore, the total force \mathbf{F}_{tot} acting on the central magnet is the sum of the forces created by the top and bottom magnets, which can be calculated with equation (3.43) if the magnets are circular and have a small radius compared to their length.

According to equation (3.43) the total force acting on the moving magnets should be the summation of two inverse quadratic functions. For the magnetic configuration of figure 4.7a,

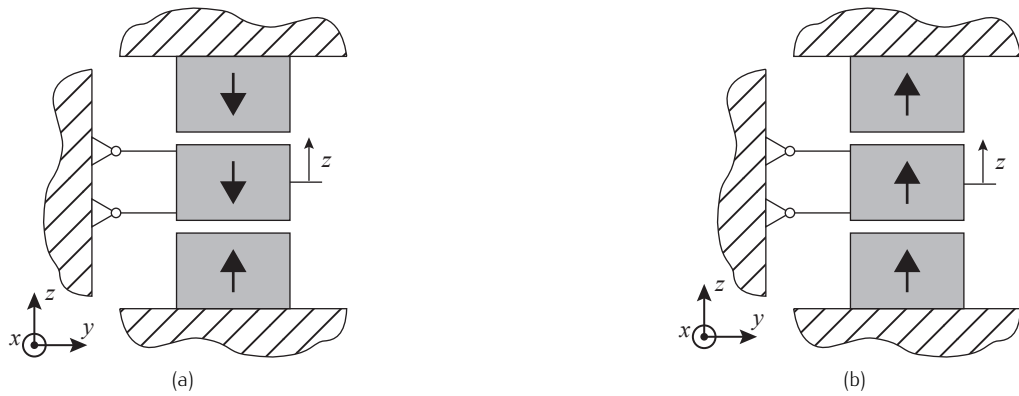


Figure 4.7: Three magnets arranged in such a way that a point of zero stiffness is created. (a) is reproduced from [3], (b) from [2]. The airgap between the magnets is of length d .

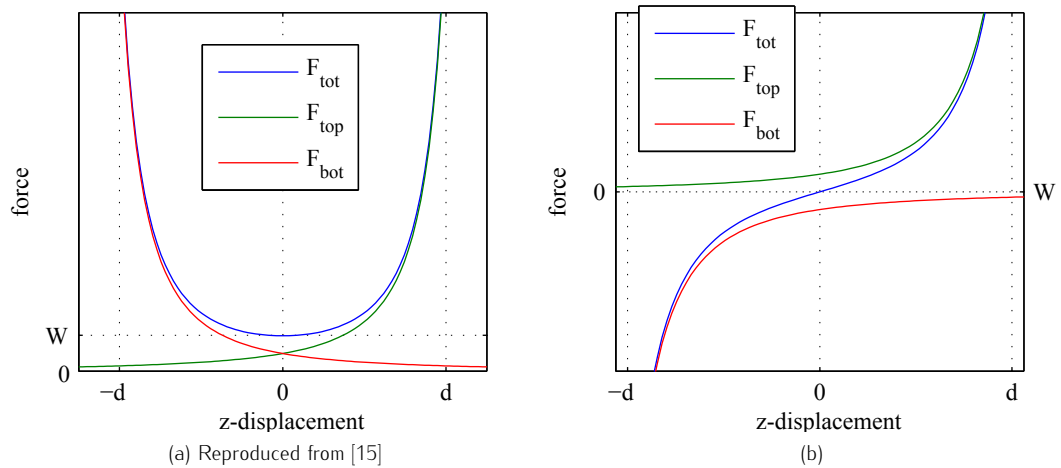


Figure 4.8: The forces-displacement curves corresponding to (a) figure 4.7a and (b) figure 4.7b. The airgap between the magnets is indicated with d , and the upwards delivered force has a magnitude W . According to (b) the concept from figure 4.7b cannot carry a weight and only adds negative stiffness.

this results in the force-displacement function shown in figure 4.8b, where we see a point of zero stiffness for $z = 0$. The magnetic typology of figure 4.7a does not result in a point of low stiffness, as shown in figure 4.8a, and is therefore only useful in a gravity compensator as compensation for some source of positive stiffness.

Square magnets

Another way of creating a gravity compensator without the use of iron, is by aligning two square magnets, with equal dimensions but opposing magnetization, so that the center of the first magnet aligns with the edge of the second, as is depicted in figure 4.9. A simulation of the forces acting on the moving magnet as function of the z -position is shown in figure 4.10. The simulated magnets are 20x20x5 mm in size and have a 1.31 T remanent flux density B_r and a 1 mm airgap between them.

The three components of the force shown in figure 4.10 in blue, green and red correspond to the forces in x, y and z -direction respectively. Because the magnetic configuration is symmetrical in the x -direction, there is no x -force acting on the moving magnet. More interesting is the force in z -direction, shown in red in figure 4.10. This force seems to become constant for

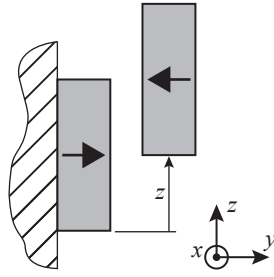


Figure 4.9: A magnet topology consisting of two repulsive square magnets, that results in a low stiffness in the z -direction. The forces corresponding to image are shown in figure 4.10. Reproduced from [3]

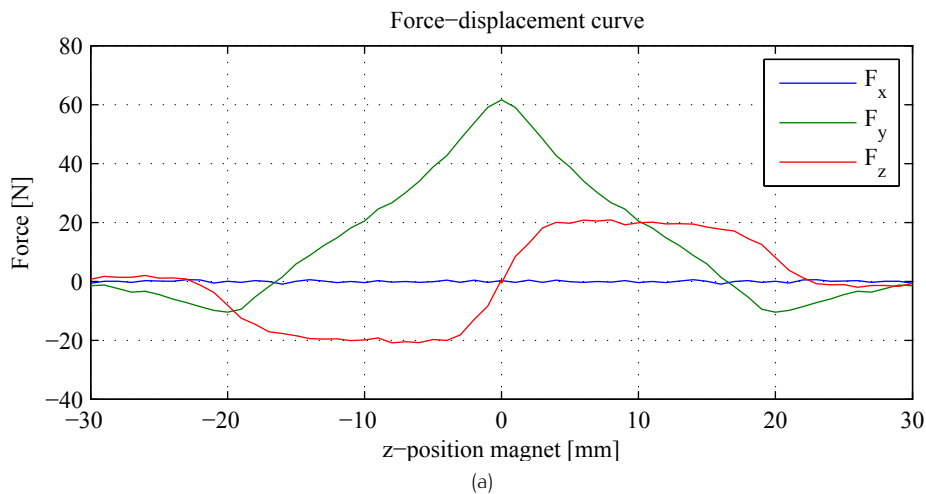


Figure 4.10: The (a) forces and (b) stiffnesses for the situation of figure 4.9, when only z -displacements are considered. The magnets are N42 20x20x5 mm with an airgap of 1mm between them. Results obtained with a 3D FEM simulation.

$3 < z < 15$. This large low stiffness region makes the concept highly suitable for use within a passive gravity compensator.

Magnetic concept choice

The “square magnets” concept is considered the best choice for a passive magnetic vibration isolation system. The concept allows for large low stiffness areas that are required to passively keep the vibration isolator in its low-stiffness working point. Also, the absence of iron in the concept reduces or removes the hysteresis effects that would be present in the iron.

4.3 Extending the square magnet concept

The “square magnets” concept from figure 4.9 is an asymmetric design and if we analyze the forces between the magnets, shown in figure 4.10, we see an unwanted force in the y -direction. One way of compensating for F_y would be by using a linear guide. However, as the forces are large in the y -direction, a strong and stiff linear guide would be needed. This linear guide would introduce a considerable amount of mechanical hysteresis, thereby rendering the whole idea of the magnet gravity compensator useless. A different—and more elegant—way of compensating for F_y is by adding a third—repulsive—magnet to the setup, as shown in 4.11a. As can be seen in figure 4.12a, this third magnet eliminates F_y while doubling F_z . Because of the symmetry in the design, there are no moments acting on the central magnet and the

moments shown in figure 4.12b are due to numerical noise.

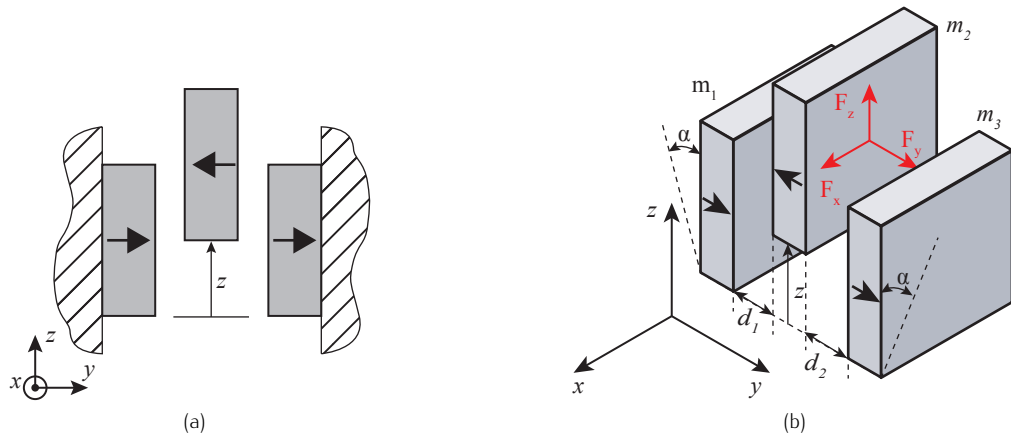


Figure 4.11: Extended version of 4.9. A third magnet is added to compensate for F_y . The magnets are numbered m_1, m_2, m_3 as shown in (b).

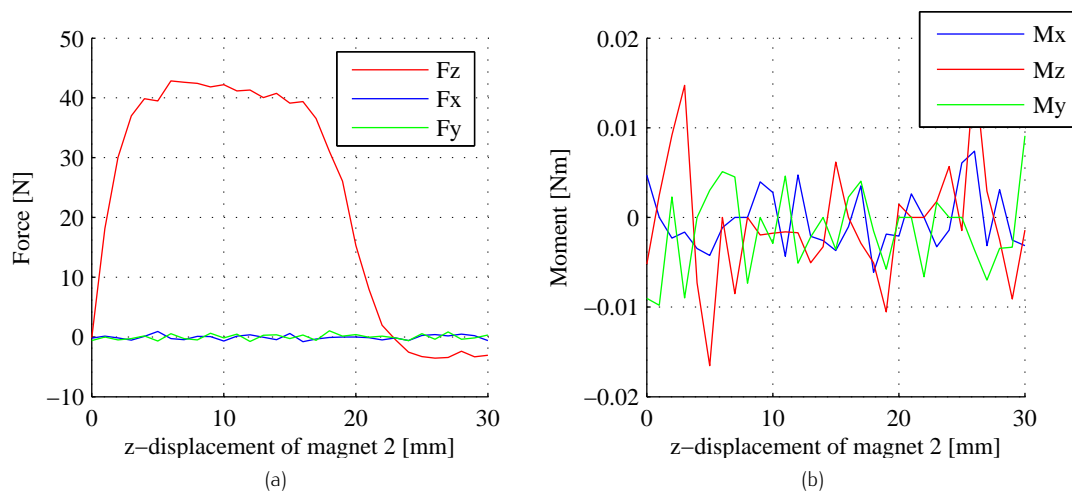


Figure 4.12: The (a) forces and (b) moments acting on the moving magnets. There is only a force in the z-direction and there are no moments. Magnets are N42 20x20x5mm with a 1 mm airgap between them.

Tunability

One of the great strengths of a vibration isolation systems such as the those made by minusk, is that they are tunable both in load bearing capacity as in stiffness. The tunability of the load bearing capacity removes the need for adding extra weight to the isolated platform, while tuning the stiffness can compensate the stiffness of for example wires going to the isolated platform; resulting is a system that is very flexible in its use. During this research is was found that both way's of tuning are also possible with the square magnets concept by adapting the airgap d and angle α of the magnets.

Tuning the load bearing capacity

The forces between two magnets are best visualized when you consider the field produced by the first magnet, and think of the second magnet a number of surface currents \mathbf{K} [A/m]. In figure 4.14 you can see two long rectangular magnets: a grey one and a transparent one with

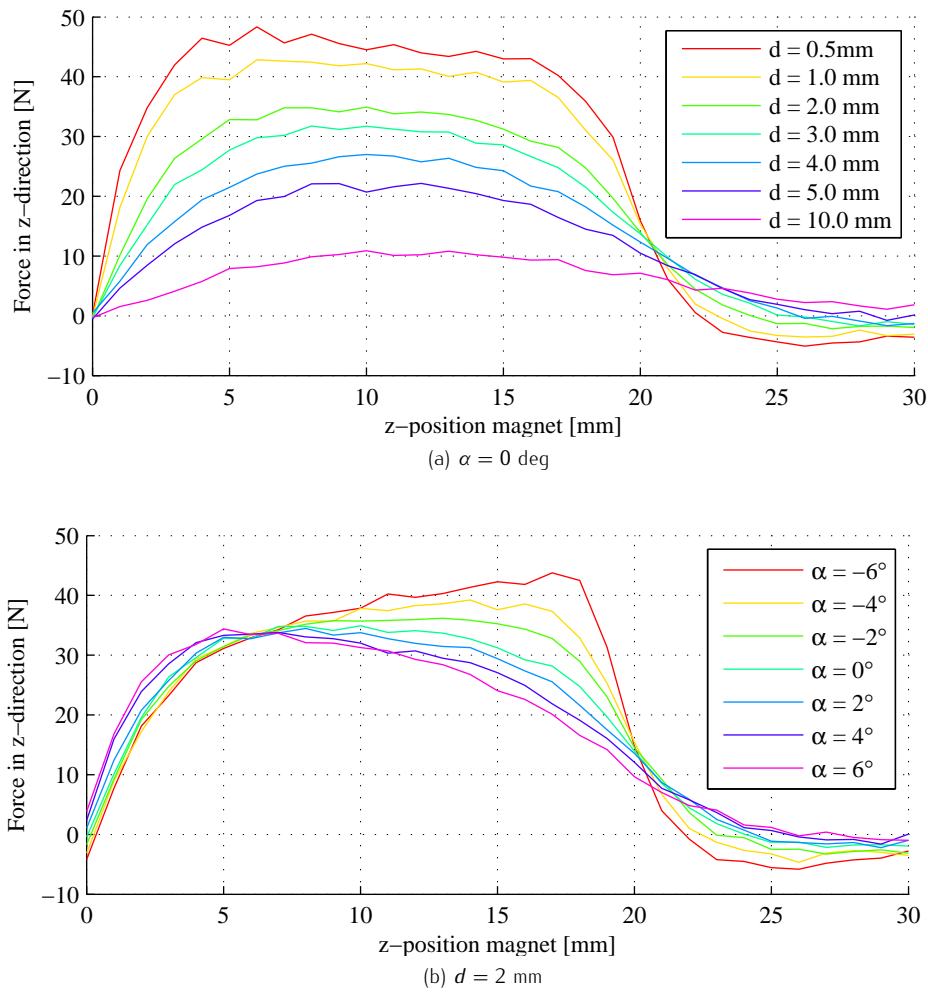


Figure 4.13: The result of a (a) change in airgap d between the magnets, and (b) change in the angle α of the static magnets. Simulations performed with N42 20x20x5 magnets.

a black outline. The thick black lines are the two current sheets that mathematically represent the transparent magnet. The magnitude of the force in x -direction—shown in red—follows from y -component of the field and is calculated using equation (3.26). When we displace the transparent magnet in the x -direction, the length of the individual force vectors changes, but their combined length remains about the same. The result is a constant force acting on the moving magnet.

If we want to increase the force, we can increase K —which would mean replace the magnet by a stronger one—or increase the field in which the surface current moves. Changing the flux density is easiest by just moving closer to the surface of the magnet where the field is stronger, so reducing the airgap d from figure 4.9 should result in a higher force acting on the middle magnet.

This experiment is validated using a COMSOL mfn simulation in 3D space and the results are shown in figure 4.13a. Reducing the airgap indeed increases the load bearing capacity as well as the size of the low stiffness area.

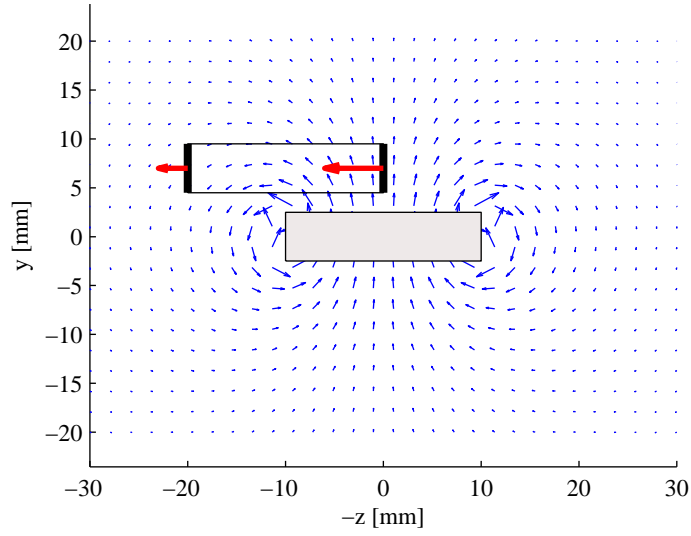


Figure 4.14: Shown is the \mathbf{B} -field created by an infinitely long rectangular magnet (grey), in which a second magnet is placed (white). The red arrows are the z -components of the forces acting on the current sheets (black lines) due to the y -component of the field. The field is calculated using equation (3.41) and equation (3.42).

Tuning the stiffness

Figure 4.13 shows that if we rotate the outer magnet with an angle α , the stiffness of the system changes. With rotations from $\alpha = -6 \dots 6$ deg, we could change the stiffness of the system from $+1000$ N/m to -1000 N/m, for a z -range of multiple millimeters.

4.4 Stability of the gravity compensator concept in all DOF

In order to be useful, the square magnets concept needs to be stable in all degrees of freedom (DOF) and unstable degrees of freedom need to be constrained. The stability conditions can be found by analyzing the total energy W_{tot} in the system. Because there is only an energy exchange between the potential and magnetic field energy, the total energy is equal to the potential energy W_{pot} and the energy stored in the magnetic field W_{fld} :

$$W_{tot} = W_{fld} + W_{pot} \quad (4.3)$$

where the potential energy is equal to the mass m of the moving part of the setup

$$W_{pot} = \int m \mathbf{g} \cdot d\mathbf{x} \quad (4.4)$$

and the magnetic energy is equal to [13]:

$$W_{fld} = \int_V \left(\int_0^B \mathbf{H} \cdot d\mathbf{B} \right) dV \quad (4.5)$$

For a soft magnetic material with a constant permeability, equation (4.5) reduces to [13, 12]:

$$W_{fld} = \int_V \frac{B^2}{2\mu} dV \quad (4.6)$$

When the system is in equilibrium, the gradient of the total energy should be equal to zero:

$$\nabla W_{tot} = 0 \quad (4.7)$$

so that the energy is at one of its extremes. If the energy profile is convex, the system is at a stable equilibrium while a concave profile denotes an unstable equilibrium point. The shape of the profile is found by taking the second derivative of equation (4.3):

$$\nabla^2 W_{tot} = \begin{cases} > 0 & \text{stable, convec, minimum energy} \\ < 0 & \text{unstable, concave, maximum energy} \\ 0 & \text{neutral, flat, constant energy} \end{cases} \quad (4.8)$$

As the force-deflections curves are already calculated with COMSOL, we can simplify our stability conditions by just looking at the derivatives of the forces and moments

$$-\nabla \mathbf{F} = \begin{cases} > 0 & \text{stable} \\ < 0 & \text{unstable,} \\ 0 & \text{neutral} \end{cases}, \quad -\nabla \mathbf{M} = \begin{cases} > 0 & \text{stable} \\ < 0 & \text{unstable} \\ 0 & \text{neutral} \end{cases} \quad (4.9)$$

where \mathbf{F} and \mathbf{M} are vectors containing the three forces and moments. The derivatives of both quantities are the translational stiffness \mathbf{k} and rotational stiffness \mathbf{c} respectively. So a positive stiffness results in a stable degree of freedom.

Translational stability

The translational stabilities are reasoned from the force-deflection curves shown in figure 4.10, figure 4.12 and figure 4.13. We can draw the following conclusions about the stability of the system:

- $k_x(x = 0) < 0$
- $k_z(\alpha, 5 < z < 15) = \begin{cases} > 0 & \text{for } \alpha > 0 \\ \approx 0 & \text{for } \alpha = 0 \\ < 0 & \text{for } \alpha < 0 \end{cases}$
- $k_y(y) > 0$

As the system will be tuned to have a slightly positive stiffness in the z-direction, only the x direction requires a added positive system: a guidance.

Rotational stability

Due to symmetry, the total rotational stability of the magnetic configuration can be investigated by looking only at rotations around the y and z -axis. The corresponding moment-rotation plots are shown in figure 4.15. From these two plots we can reason that:

- $c_x = c_z > 0$
- $c_y = \begin{cases} < 0 & \text{for } R_y < 20 \text{ or } R_y > 70^\circ \\ > 0 & \text{for } 20^\circ < R_y < 70^\circ \end{cases}$

As the moving magnet is not rotated about the y -axis ($R_y = 0^\circ$) the stiffness $c_y < 0$ and the DOF is unstable and requires an additional positive stiffness.

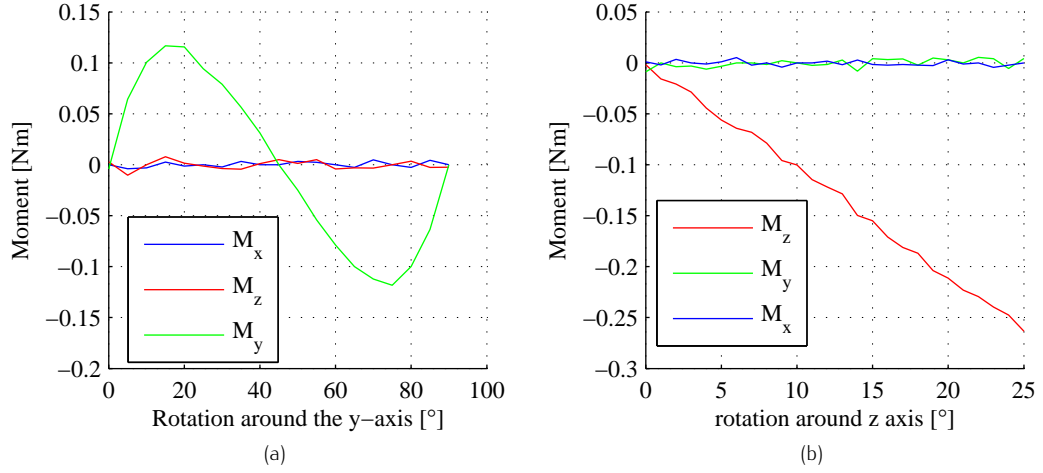


Figure 4.15: The moment-rotation curves for (a) a rotation about the y -axis and (b) about the x/z -axis.

Earnshaws Law

From section §4.4 the question arises if it is possible to compensate for the instabilities in the x and R_y directions by adding more magnets or using other sizes or shapes of magnets. The answer is no, stable levitation is not possible using just static magnetic or electric fields. The cause is that the second derivative of the magnetic potential $\nabla^2 W_{fld}$ will be zero, meaning that the potential field has an unstable saddle shape. This is often called Earnshaw's theorem, although Earnshaw never wrote about magnetic fields and his work was still based upon dated physical concepts such as the existence of luminous ether [24]. Three elaborate and far more recent proofs are found in [25, 26, 5].

4.5 Influence of alignment errors or non-symmetries

When the square magnetic gravity compensator concept is implemented in a setup, it is most likely that the magnets are not perfectly aligned. The following three alignment errors are examined:

1. There is a difference in the x -alignment of the non-moving magnets m_1 and m_3 (see figure 4.11b);
2. There is a difference in the x -alignment of the non-moving magnets (m_1, m_3) and the moving magnet m_2 (see figure 4.11b);
3. There is an uneven airgap between the magnets, so that $d_1 \neq d_2$ (see figure 4.11b).

The influence that each of these three miss alignments has on the force and moment curves of the magnetic gravity compensator, is discussed in the following paragraphs.

x - alignment error between m_1 and m_3 Figure figure 4.16 shows the forces as function of the z -displacement of the moving magnet, when there is an x -alignment error between the two

outer non-moving magnets. Two parasitic forces $F_x(z)$ and $F_y(z)$ appear, but the alignment error has little influence on the load bearing capacity of the setup. The same figure shows two parasitic $M_y(z)$ and $M_x(z)$. An x-alignment error between the outer magnets can be avoided by placing them in a stiff enclosure, machined with high tolerances, which is done in the final design of the demonstrator (see figure 6.7 on page 56).

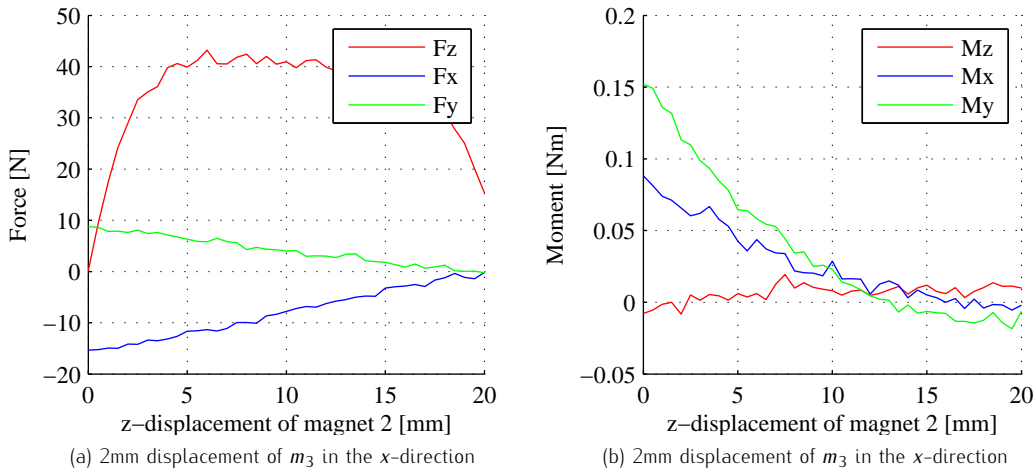


Figure 4.16: The parasitic forces acting on the moving magnet m_2 , as result of senario 1: an uneven x-position of magnets m_1 and m_3 .

x-alignment error between m_1, m_3 and m_2 A more probable alignment error is the x-alignment error between the two outer magnets and the moving magnet. Figure figure 4.17 shows that an alignment error of 2 mm will result in a maximum force in x-direction of almost 30 N, as well as a moment around the y-axis. These forces and moments will be used in chapter 6 and section §A.1 as buckling requirements for the linear guide.

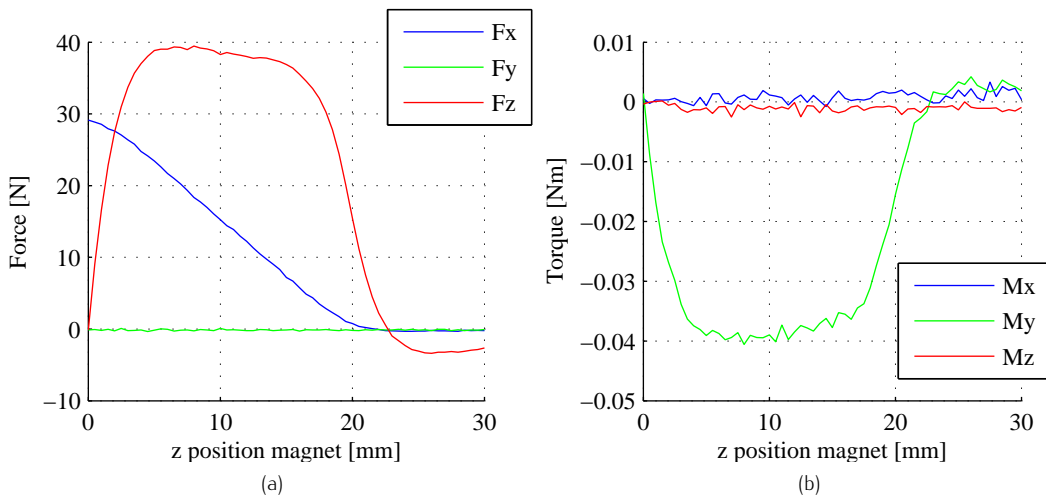
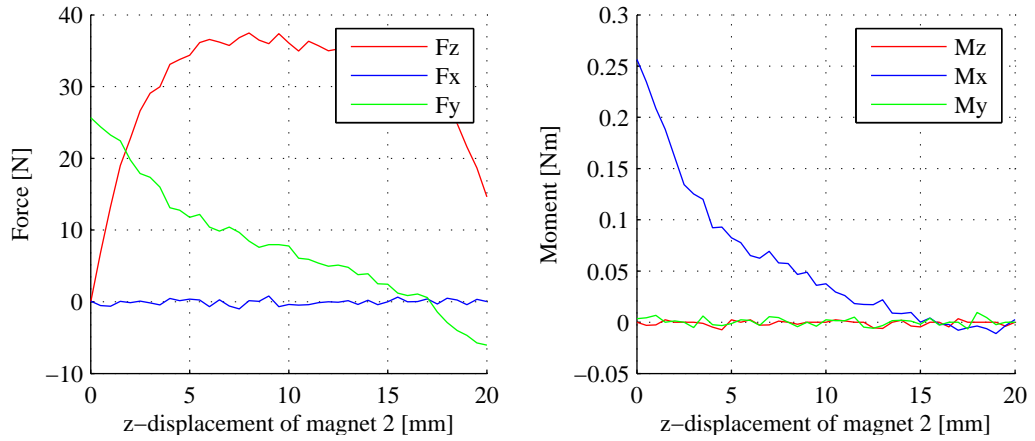


Figure 4.17: (a) The forces and (b) the moments corresponding to an x-alignment error between the two outer magnets and the moving magnet of 2 mm.

Uneven airgap between the magnets ($d_1 \neq d_2$) An uneven airgap between the magnets results in a large force in y-direction and in a large moment around the x-axis, as is shown in figure 4.18. The force F_y tries to equalize the airgaps between the magnets such that

$d_1 = d_2 = d$. When the linear guide of the moving magnet has a low stiffness in the y -direction, the moving magnet can magnetically align itself in y -direction. This is done in the final design of the demonstrator by means of flexure hinges, as shown in figure 6.5 on page 55.



(a) 2mm displacement of m_3 in y direction ($d_1 = 1\text{mm}$ and $d_2 = 3\text{mm}$) (b) 2mm displacement of m_3 in y direction ($d_1 = 1\text{mm}$ and $d_2 = 3\text{mm}$)

Figure 4.18: The parasitic forces acting on the moving magnet m_2 , as result of scenario 3: an uneven gap size ($d_1 \neq d_2$)

4.6 Conclusion

The magnetic gravity compensator concept needs to have a low stiffness and contain little damping, while having a minimum number of unstable degrees of freedom. It was found that the 'square magnet' concept meets these requirements best. The square magnet concept consists of three rectangular magnets and can be used to create a gravity compensator with a low stiffness over a large range of approximately 1/2 of the magnets height. When 20x20x5 mm N42 neodymium magnets are used, this results in an expected load bearing capacity of $\approx 40\text{ N}$ over a range of $\approx 10\text{mm}$. As the gravity compensator does not contain any iron, little damping is expected. Fine tuning the load bearing capacity of the system can be done by controlling the airgap, while the stiffness can be made both positive and negative by tilting the outer two magnets. The magnetic configuration is unstable for translations the x -direction and for rotations R_y around the y -axis, making a linear guide with low stiffness and damping in the z -direction necessary. This linear guide should also have a low stiffness in the y -direction, while having a high stiffness in the x -direction, to compensate for the forces that result from small alignment errors of the permanent magnets.

Gravity compensator validation

The previous chapter discussed the conceptual design of the magnetic gravity compensator, and analyzed its performance using finite element software. This chapter discussed the test setups used to measure and validate the performance of the gravity compensator. The validation process is an extra step taken to ensure that the gravity compensator behaves as expected, before it will be implemented in the demonstrator as described in the next chapter.

The validation process of the gravity compensator consists of two parts. In the first part, the field of the magnets is measured to determine its remnant flux density and dimensions, which is not as straightforward as it sounds, while in the second part the force–displacement curve is measured for multiple airgaps.

5.1 Validating the B-field of a square magnet

The first step in validating the simulation results of section §4.3 is validating the B-field of a permanent magnet, as the force acting on a magnet depends upon the magnetization of the magnet and the strength of the B-field in which it is placed. This B-field created by a permanent magnet is a function of the remnant flux density B_r as well as the dimensions of the magnet and the position \mathbf{x} where the field is observed. So in order to validate the B-field, we need to validate the remnant flux density and the dimensions of the magnets, which is not as straightforward as directly measuring them.

The dimensions of a magnet are given by a supplier and can ofcourse be checked with a calliper. However neodymium magnets contain a coating of unknown thickness that protects the brittle magnetic material inside. So when using a calliper you do not measure the dimensions of the dimensions of the magnetic material, while that is what you would like to know.

The remnant flux density of neodymium is indicated by the class of the magnet. In this reasearch neodymium magnets of class N42 are used, which should have a remnant flux density between 1.29 and 1.32 T. This results in a $\pm 2.3\%$ uncertainty in the remnant flux density. A second problem is: how do you measure this remnant flux density. As remnant flux density $1.29 < B_r < 1.32$ T does not mean that the field that you measure at the magnet surface should be between these values.

Fitting the flux B-field measurements

A way to obtain the dimensions and remanent flux density of a magnet, is by measuring the B-field at the centerline of the magnet. This data can then be fitted to the one-dimensional model of equation (3.40). Results of the measurement and a fit are shown in figure 5.1a. The B-field is measured with the Magna MG-701 Gauss meter and the observation positions \mathbf{x} are prescribed by the 3D printed checkerboard shown in figure 5.1b. As there are only two unknown variables—the coating thickness s and remenant flux density B_r —a trial and error

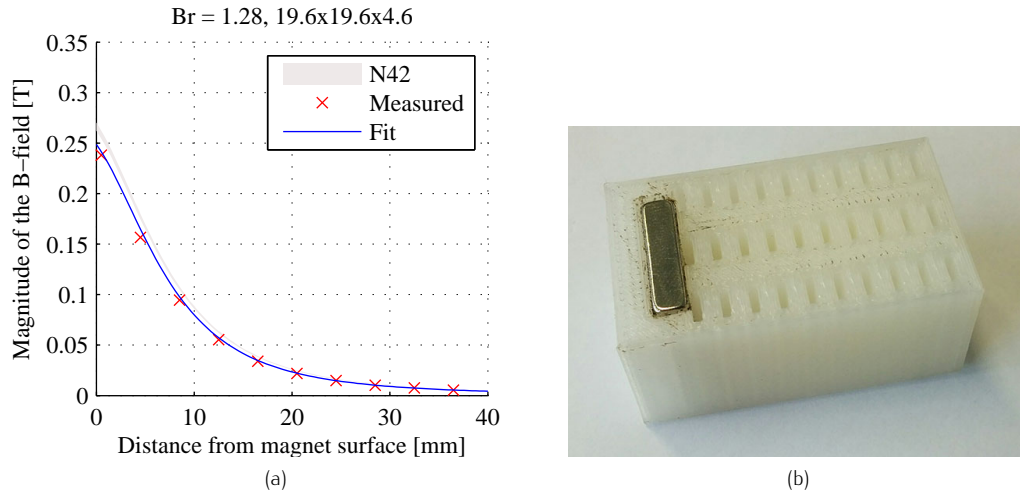


Figure 5.1: The magnitude of the field on the centerline of the permanent magnet is shown in (a). The measurement points are shown in red, while the blue line is calculated using equation 3.40 on page 24. The measurement results are used to determine the unknown parameters in equation (3.40) ($B_r = 1.28$, $w = l = 19.6$ mm, $h = 4.6$ mm). (b) Shows a 3D printed checkerboard with 3×10 holes in it. The field is measured in the holes using the Magna MG-701 Gauss meter.

approach was used to fit the model. A remanent flux density of 1.28T and a coating thickness of $200\mu\text{m}$ were found to result in an accurate fit, where the coating thickness is assumed to be identical at all sides of the magnet.

5.2 Validating the force-displacement curve

Description of the measurement setup

The force-deflection curves of figure 4.13 are validated using the setup shown in figure 5.2a,b,c. The setup is completely built using only rapid prototyping and out-of-the-box Thorlabs parts and consists of the following components:

- two Thorlabs kinematic mounts that contain two static magnets (figure 5.2b);
- a plexiglas linear guide for the moving magnet (figure 5.2b);
- a Thorlabs manual 1D stage;
- an opto NCDT 1401 laser triangulation sensor;
- a FUTEK 10 lb (44.5 N) load cell.

The moving magnet is placed in a plexiglass enclosure that can move in the plexiglass linear guide, both produced by laser cutting. The friction in the linear guide is decreased by applying a Teflon coating to the plexiglass. This decreases the friction to less than 0.4N, as can be seen in figure 5.2.

The force acting on the central magnet is measured using a FUTEK load cell that is rated for use up to 10lb, or 44.5N. The connection between the magnet and the load cell consists of a non-magnetic steel wire. Measuring the displacement is done using an opto NCDT 1401 laser triangulation sensor. To avoid any influence of the deformation of the steel wire due to the magnetic forces, the displacement is measured directly at the enclosure of the moving magnet.

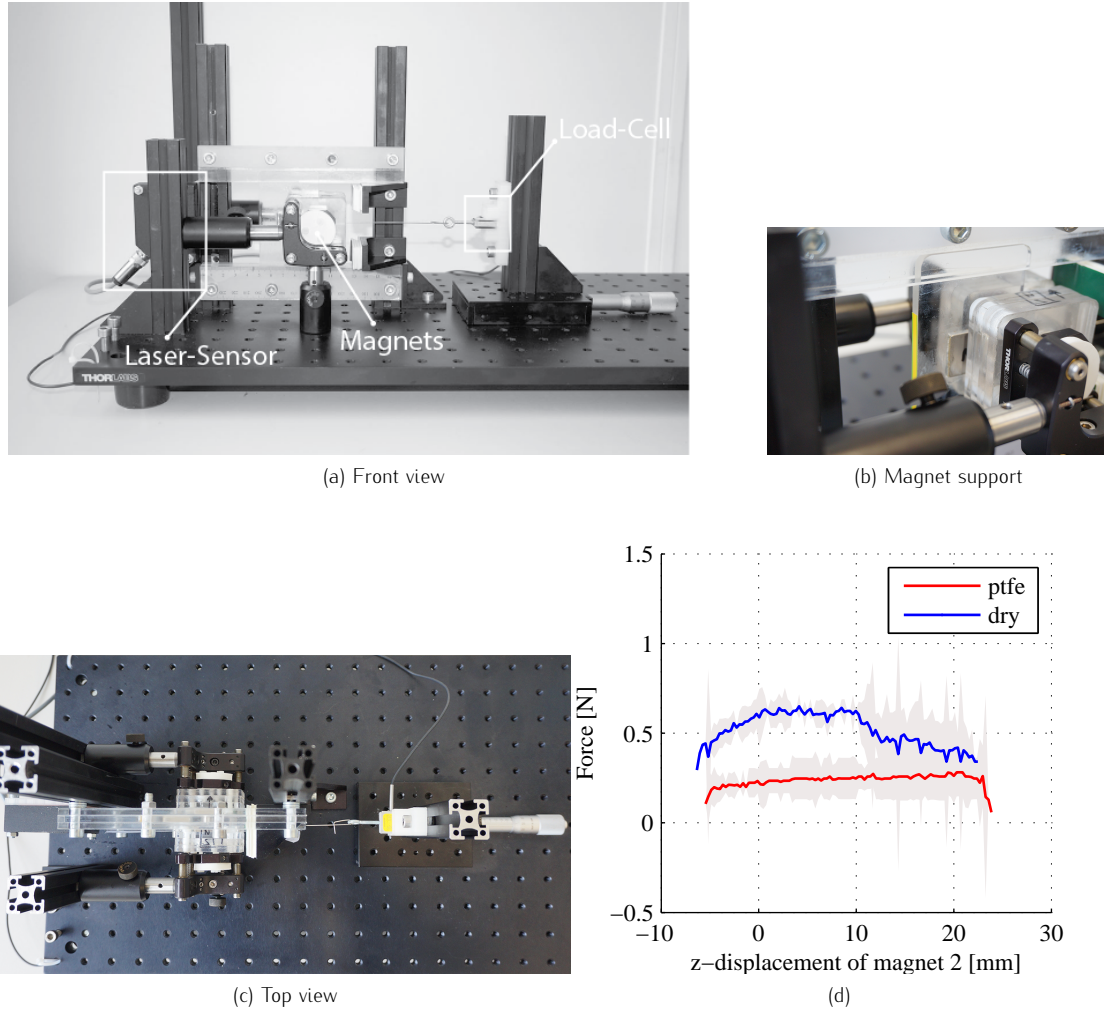


Figure 5.2: The setup used to verify the force-displacement curves of figure 4.13 is shown in (a) to (c). You can see the magnet enclosures, the plexiglass linear guide, the load cell and the laser triangulation sensor. The friction of the linear guide is shown in (d), where the blue and red lines are the average friction force measured before and after applying a teflon coating to the plexiglass. The grey area's are the 3σ standard deviations of 4 force measurements. .

The Thorlabs 1D stage is used to impose a displacement on the moving magnet and limits the range of the setup to 25 mm.

The two non-moving magnets are enclosed in two plexiglass casings and mounted on two thorlabs kinematic mounts. Three screws on these mounts are used to adjust the airgap d and magnet angle α . Stacks of 0.5 mm thick aluminum plates are placed between the magnets during adjustment to ensure the desired airgap.

Force-displacement curve for $\alpha = 0$

When the angle α of the outer magnets is zero, we expect to measure a force with a low stiffness area of zero to ten millimeters, depending on the airgap d . The measurement setup is used to validate the force-displacement curves corresponding two and five millimeter airgaps. .

The measured force-displacement curve $F_z(z, d = 5)$ corresponding to an airgap of 5 mm is shown in figure 5.3a. In this figure, the red line is the mean result of three measurement while the grey area is the mean result plus three times the standard deviation σ of the data. Because of the high repeatability of the measurement, there is a small standard deviation. We can see

that the profile of the measured force is very similar to the COMSOL simulation result, but that the value of the measured force is about 15% lower than the simulated force at its maximum value. The most likely explanation for this difference is that the airgap was slightly larger than two millimeter. This small error in the position can result in a large error in the force, because the field decreases quadratically with the position. So a small position error becomes a quadratic error in the force. The stiffness-displacement curve $k_z(z, d = 5)$ corresponding to the five millimeter airgap is shown in figure 5.3b and there is only a point of zero stiffness, which agrees with the expectations.

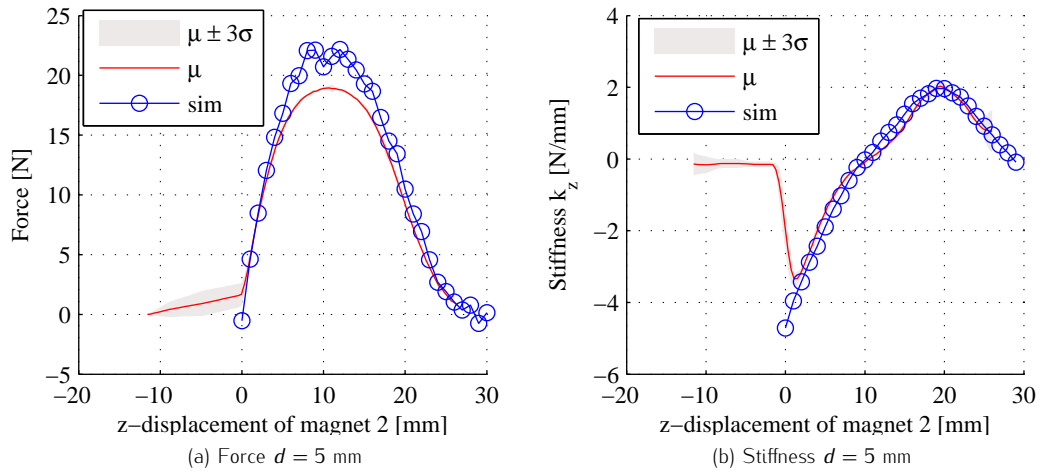


Figure 5.3: The measurement results and simulation results for an airgap of 5 mm. (a) shows the force-deflection curve and (b) shows the corresponding stiffness. Measurement and simulation results show great resemblance.

In case of a two millimeter airgap, we expect to see a zero stiffness region of about five millimeter. However, the measurement results of figure 5.4a,b show something different. Not only is the force more than 15% lower, but also the zero stiffness region is larger than expected. How is this possible? Well, the most likely cause is the limited stiffness of the Thorlabs mounts holding the two non-moving magnets. Because the airgap is smaller, the forces in the y -direction are far larger. These forces are large enough to deform the Thorlabs mounts, thereby creating a larger airgap that reduces the force F_z . This limited stiffness of the setup made it impossible to perform measurements with even smaller airgaps.

Because both the stiffness and the force in z -direction are known, it is possible to calculate an eigenfrequency. When we say that the mass of the setup is equal to the force divided by the gravity, the equation for the eigenfrequency becomes:

$$f_n = \frac{1}{2\pi} \sqrt{\frac{k_z g}{F_z}} \quad (5.1)$$

where f_n is in Hz. The eigenfrequency-displacement curve corresponding to the two millimeter airgap is shown in figure 5.4c. The above equation is only useful for the part of the curve where the stiffness is positive. When the stiffness is negative the real part $\Re(f_n)$ becomes zero and the function becomes imaginary, which can also be seen in figure 5.4c. This problem is solved by slightly tilting the outer magnets by an angle α , so that the stiffness becomes positive.

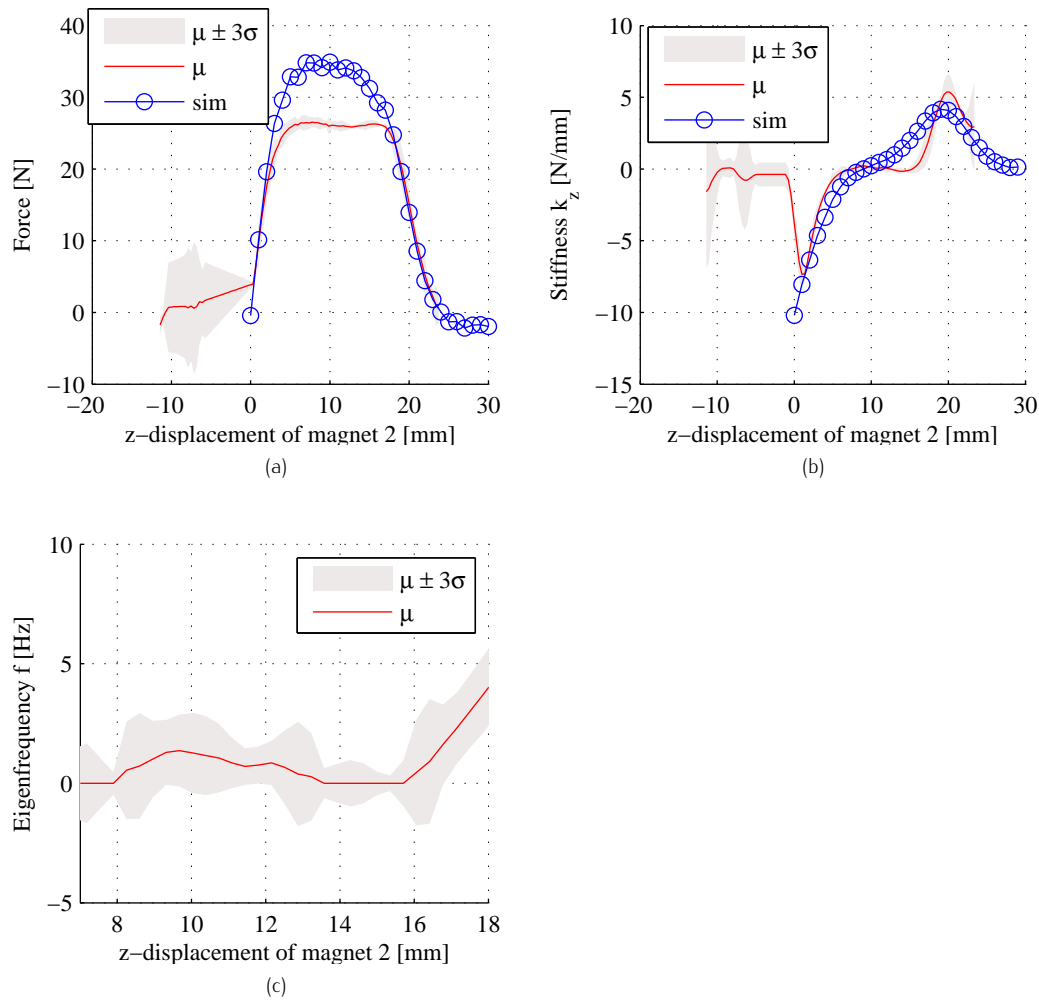


Figure 5.4: The measurement results and simulation results for an airgap of two millimeters. (a) shows the force in z-direction (b) shows the stiffness and (c) the eigenfrequency.

Force-deflection curve for $\alpha \neq 0$

Due to the low stiffness of the support of the two non-moving magnets, it was not possible to perform useful measurement for $\alpha \neq 0$. The phenomena of figure 4.13 is only seen for smaller airgaps, but at these smaller airgaps the forces and torques acting on the supports cause deformations that make it impossible to accurately position the magnets under a certain angle α .

5.3 Conclusion

The B-field of a permanent magnet is measured using a Gauss meter and a 3D printed checkerboard. By fitting the measurement data of the B -field to equation (3.40), it was found that the neodymium magnets used in this research have a remnant flux density of 1.28T and a coating thickness of $200\mu\text{m}$. Rapid prototyping and out-of-the-box parts were used to create a setup, with which the force-displacement curves of the gravity compensator were measured for different airgaps. The measured load bearing capacity of the gravity compensator was found to be up to 20% lower than the COMSOL simulations predicted, which could—at least partly—be explained by the limited stiffness of the mounts in which the outer two magnets

where placed. The overall shape of the force displacement curves showed enough resemblance with the COMSOL simulation results to consider the simulation results of chapter 4 useful, and use the square magnetic concept as gravity compensator in the demonstrator. The limited stiffness of the magnet mounts made it impossible to place—and keep—the magnets under a small angle to validate the tunability of the stiffness. .

Part III

Demonstrator design and performance evaluation

Demonstrator design and performance evaluation

The previous chapter discussed the validation of the magnetic gravity compensator. This chapter will focus on the demonstrator, which is the proof-of-concept vertical vibration isolator that implements the passive magnetic gravity compensator. The chapter starts with an overview of the functions and requirements of the demonstrator, followed by a discussion of its design. Finally, the performance of the demonstrator is evaluated by means of static and dynamic measurements.

6.1 Functions and requirements of the demonstrator

The main function of the demonstrator is to vertically suspend a mass with low stiffness and little damping, using the magnetic gravity compensator discussed in the two preceding chapters. As explained in chapter 4, this means that the setup should position two magnets at a certain angle α and with a certain airgap d , while a third magnet can move between those two magnets¹. The gravity gravity compensator can be thought of as a nonlinear magnetic spring k_m that supports a mass, and has a low stiffness for only a certain range. As explained in section §4.3 and validated in chapter 5, we need to position the system at a point within in this range and only allow motion around this point.

The above can be translated to the system shown in figure 6.1. The mass m_1 represents the vibration isolated platform, which is suspended by the magnetic spring k_m . A linear guide with stiffness k_s and damping c_s is connected to the mass m_1 and is used to stabilize the magnetic gravity compensator. This linear guide is also connected to a second body m_2 , that can be positioned at a certain height z_2 to place the magnetic spring in its low stiffness region. The system is kept in this low stiffness region by mechanical end stops. Adjusting z_2 is done with a stiff spindle, so the dynamics of the system shown in figure 6.1 simplify to those of a simple mass-spring-damper system.

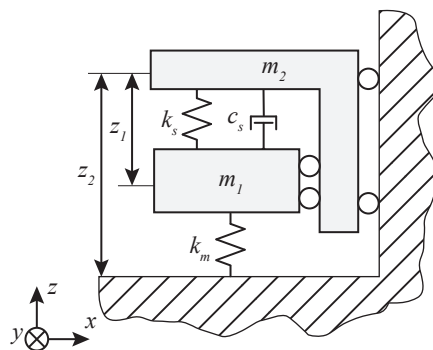


Figure 6.1: Schematic drawing of the demonstrator. z_2 is enforced by a spindle, reducing the dynamics to those of a simple mass-spring-damper system.

¹The exact definition of α and d is illustrated in figure 4.11 on page 36.

Now the design of the demonstrator is translated into an number of components, we can define requirements for each separate component. These requirements are:

- The linear guide of m_2 should be able to position the system at any point of the force-displacement curve that has a low stiffness. According to figure 4.13 and figure 5.4 this means that $z_2 = 4.0 \dots 16.0$ mm.
- The stiffness k_s of the linear guide of m_1 should be smaller than 1000 N/m, which is the maximum achievable negative stiffness of the magnetic spring according to figure 4.13b.
- The damping c_s should be minimal
- The range of the linear guide of m_1 should be at least $z_1 = -5 \dots 5$ mm in order to use the system in its complete expected low stiffness area.

Apart from these requirements, there are also two requirement for the positioning of the magnets:

- The airgap d should have a range of $0.5 \dots 2 \pm 0.1$ mm, because the force-deflection curve of the magnet configuration has a clear low stiffness region for this range. The accuracy of 0.1 mm follows from the numerical noise of the COMSOL simulation.
- The angle α should have a range of $-6 \dots 6 \pm 0.3$ deg. At a 6 deg angle, the positive or negative stiffness is approximately ± 1000 N/m, which should be enough to compensate for the stiffness of the linear guide.

6.2 Design of the demonstrator

The completed demonstrator is shown in figure 6.1. In this image we can see a cubical frame on which all components are mounted, with a box hanging beneath it that serves as an adjustable mass. The upcoming sections will explain the most important choices in the design.

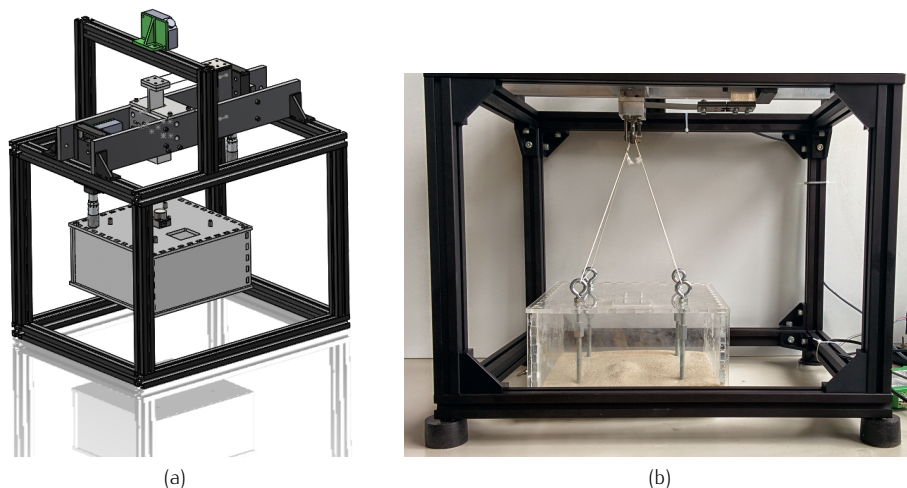


Figure 6.2: (a) A rendering of the demonstrator and (b) a picture of the demonstrator

Platform position

One of the most influential choices made during the design process is the position of the vibration isolated platform, which is located below a single magnetic spring instead of above it. From a practical point of view it would make more sense to place the isolated platform above the zero stiffness suspension, like is done in most commercial systems. This way it is easier to place components atop the isolated platform, without the system itself being in the way. The downside from this layout is that—when the center of gravity is located above the suspension—three zero stiffness contact points are needed. Because the goal of this research is to create a demonstrator—and not a commercial product—it is chosen to use the simpler but less practical layout and mount the platform directly beneath a single magnetic zero stiffness spring.

Linear guides

There are two linear guides used in the demonstrator, both shown in figure 6.5. The first linear guide is a manual 1D stage and is used to adapt the 'pre-tension' z_2 of the magnetic spring (see figure 6.1). We would like to do this, because the low-stiffness area is confined to certain elongations of the of the magnetic spring. Outside of this area, the magnetic spring is very stiff and not suited for use within a vibration isolation system.

A second linear guide allows the central magnet to move vertically in its low stiffness area. Flexures are used instead of bearings because of their predictable and repeatable behavior and their lack of backlash. Figure 6.3 shows the four flexure-based linear guides considered during the design process. The simple double flexure linear guide concept of figure 6.3a is used in the design.

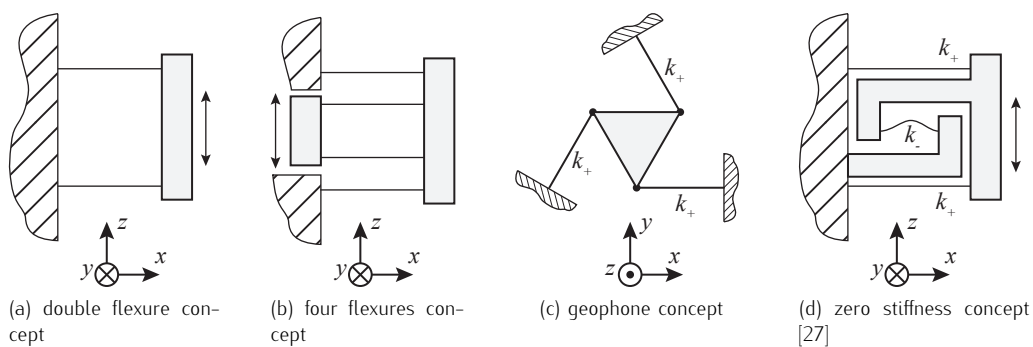


Figure 6.3: Four flexure-based linear guides that could be used in the design. Option a) is used in the demonstrator.

A downside of the double flexure concept is that the x -position of the moving body depends upon its z -position, which is unwanted because the force curve of the magnetic spring also depends upon the x position of the magnet. The x – z dependence could be removed by adding a second pair of flexures, connected to an intermediate body, as shown in figure 6.3b. When the second pair of flexures is equal in length and stiffness, they completely cancel out each others x -displacement. However, the extra mass required as intermediate body—schematically shown in figure 6.4—introduces a second eigenfrequency in the system. Because of the relatively low mass m_i of the intermediate body, this new eigenfrequency will be at a higher frequency, strongly degrading the performance of the system.

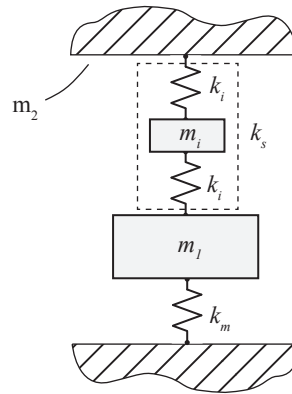


Figure 6.4: Dynamic model that shows why a linear guide with an intermediate body is a bad idea.

A third option is to use steel wire flexures instead of leafsprings. Each wire locks a single degree of freedom, so three wires can remove all planar motion when arranged as in figure 6.3c. By stacking a second set of wire flexures on top of the first we create a system that allows motion solely in the z -direction [28]. Because this type of linear guide is used in geophones, it is called the geophone concept. A downside of the geophone concept is that a translation in z -direction results in a parasitic rotation R_z about the z -axis. In chapter 4 it was explained that the magnetic concept has a high rotational stiffness around its x and z -axis. If the geophone concept would be used, this rotational stiffness would be coupled to the translational stiffness k_z through the linear guide, making also this concept unsuited.

The fourth and final concept is consist of two flexures with a positive stiffness and a buckling beam with a negative stiffness, as shown in figure 6.3d. This concept is know to have a low combined stiffness but also has a coupled $x - z$ motion. As the linear guide only needs a stiffness lower than 1000N/m, there is no reason for using this complex system instead of the much simpler 'double flexure' concept.

Because of the reasons mentioned above, a double flexure is considered the best option for the linear guide and is implemented as shown in . The used flexures have a length of 65 mm, a width of 40 mm and a thickness of 0.2 mm and provide a good balance between stiffness, buckling force and range. Two sets of flexures have been used, a first with a combined calculated stiffness is 489 N/m and has been measured to lie between the 422 N/m to 424 N/m—depending upon the measurement method used—and a second with a calculated stiffness of 61 N/m. More about the dimensioning and validation of the linear guide can be read in section §A.1 of the appendix.

The magnetic spring has a high stiffness in the y -direction because the magnets are repulsive. This would cause an overconstrained system, as the leafsprings also have a high stiffness in the y -direction. Flexure hinges are added to the leaf springs—as shown in figure 6.5—to lower the mechanical stiffness. The x -position of the moving magnet can be adjusted up to a few millimeters using the 3 adjustment screws and 2 spring loaded bolts shown in figure 6.5.

Positioning the magnets

We like to position the two magnets that form the non-moving part of the magnetic spring with a high stiffness and sufficient pre-tension, while still being able to adjust the airgap d and magnet angle α . Figure 6.6 shows the load acting on the positioning system as function of the airgap, for two z -displacements of the moving magnet. These load cases are selected because

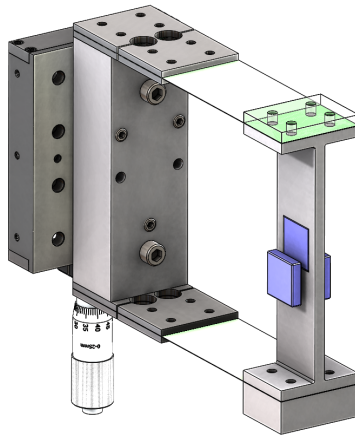


Figure 6.5: The Thorlabs stage and the two leafsprings. Flexure hinges are added to give the system a low mechanical stiffness in the y -direction. The two non-moving magnets are shown without their enclosure to clarify the arrangement.

the system will be used at $u_z \approx 10$ mm, while the force in y -direction will be maximum at $u_z = 0$. From figure 6.6a we can conclude that the y -stiffness of the system needs to be in the order of $6 \cdot 10^5$ N/m to meet the positioning requirements, while figure 6.6b shows a magnetic pre-tension in y and z -direction for all airgaps. This means that we only need to apply a force in x -direction to keep the magnets on their place.

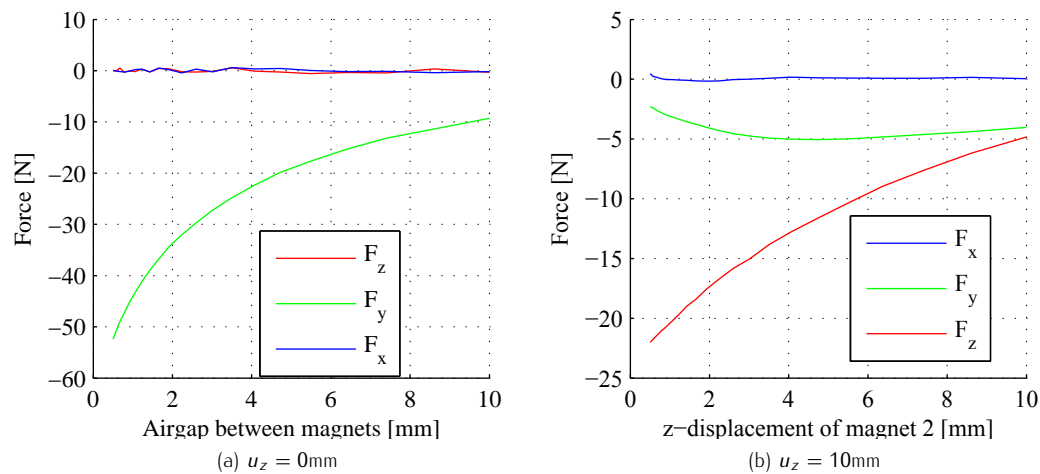


Figure 6.6: The force acting on magnet m_1 of figure 4.11 on on page 36

A positioning system that allows continuous adjustments to the airgap and angle of the airgap would be preferable for a commercial product, but also adds a lot of complexity to the design while not adding much academic value to the project. Therefore it was chosen to place the magnets in a aluminum enclosure that is positioned against six spheres as shown in figure 6.7, creating a kinematic mount.

The airgap is adjusted in steps of 0.5 mm with aluminum plates between the spheres and the aluminum enclosure, while the angle of the magnet could be adjusted with different sets of aluminum enclosures. Switching between different sets of magnet enclosures is no problem because the kinematic mount has a very high position repeatability in the order of micrometers.

The stiffness of the hertz contact in the order of 10^7 N/m and is given by [27]:

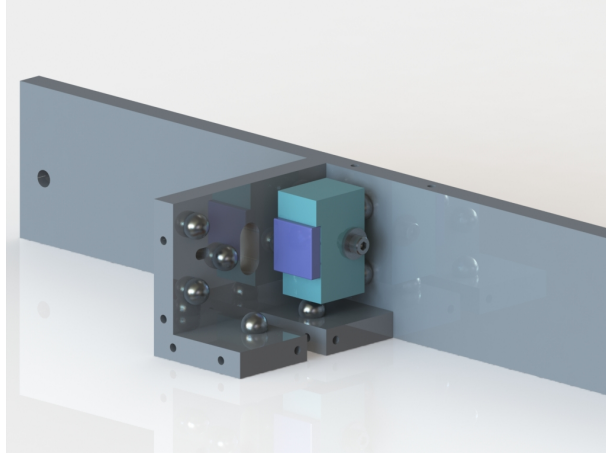


Figure 6.7: The positioning system of the magnets. The magnet (blue) is glued into its enclosure (green) and pressed against the metal 6 spheres by a spring-loaded screw. Pre-tension in y and z direction is provided by the repulsive forces between the magnets. Only one magnet is shown.

$$k = {}^3\sqrt{\frac{4}{9}rF_{axial}E_{eq}^2} \quad (6.1)$$

where E_{eq} is the equivalent stiffness of the ball (E_1, ν_1) and flat (E_2, ν_2):

$$E_{eq} = \left(\frac{1 - \nu_1^2}{2E_1} + \frac{1 - \nu_2^2}{2E_2} \right)^{-1} \quad (6.2)$$

making the system stiff enough for reliable measurements.

6.3 Static force measurements

The measurement setup used to validate the force curves is shown in figure 6.8. Shown are the magnet in a 3D-printed enclosure directly connected to the loadcell, which is in turn connected to a 1D stage. The position of the magnet is measured directly at the magnets enclosure, using a OptoNCDT 1402-50 laser triangulation sensor. The loadcell is a vishay 1006, which is a single point load cell with a measurement range up to 50 N.

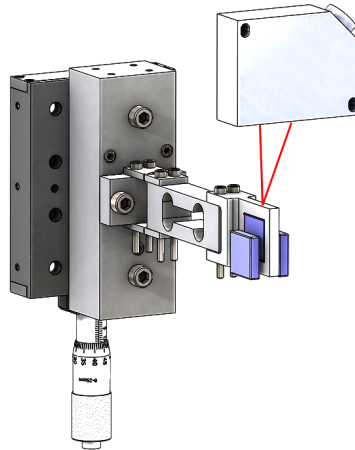


Figure 6.8: The leafsprings are replaced by a single point loadcell for the force-displacement measurement. The magnet is directly attached to the load cell and its z -position is measured by a laser triangulation sensor. Results of the measurement are shown in figure 6.9.

Single point load cells have the advantage over other types of force transducers that they are only sensitive in one translational degree of freedom, because they are essentially linear guides. The high stiffness and low sensitivity of the load cell for all rotations and two translation removes the need for a linear guide during the force measurement, making it possible to measure just the force caused by the magnetic spring, without parasitic forces caused by a guidance system. The measurement results for an airgap of 0.5 mm, 1.0 mm and 2.0 mm are shown in figure 6.9.

When comparing the measurement results from figure 6.9 with the simulation results of figure 4.13 and measurement results of figure 5.4, we see two large differences: the forces are lower than expected and the shape of the seems distorted. The force curve in case of a 0.5 mm airgap is shown in 6.9a and is only reasonable flat between 6 and 9 mm. For larger deformations of the magnetic spring, the force increases rapidly, resulting in a large and unexpected negative stiffness.

The other two force curves show similar behavior. At an airgap of 1.0 mm the low stiffness area starts at a deformation of 6 mm and has a length of only 1.5 mm, while at an airgap of 2.0 mm there is no low stiffness area at all. Again the measurement results do not agree with earlier simulations and measurements. What could cause this large difference?

The answer is probably the metal used in the setup. Although almost all components are produced out of aluminum, there are small steel spheres used in the kinematic mount shown in figure 6.7. During the design it was assumed that these spheres would be small enough and located far enough from the magnets to have no significant influence on the force curve. But from the measurement results of figure 6.9 we can conclude that this assumption was wrong and that the ferromagnetic material does have a detrimental effect upon the performance.

The metal spheres are positioned slightly below the center of non moving magnets and have a radius of 5 mm. The magnetic field in the air gap between the magnets is decreased within this range because the magnetic flux prefers to travel through the steel instead of through the air because of the lower reluctance of the steel. As result, the force acting on the moving magnet decreases. The influence of the metal sphere reduces at larger deformation of the magnetic spring, resulting in a stronger field and thus explaining the peak in force around 18 mm.

Due to time constraints, it was not possible to order spheres made of a material with a lower permeability, such as anodized aluminum or other types of stainless steel and redo the measurements of figure 6.9.

Tuning the stiffness

Force measurements with the outer magnets under an angle α have neither been conducted, because tuning the stiffness of a non-constant stiffness makes no sense.

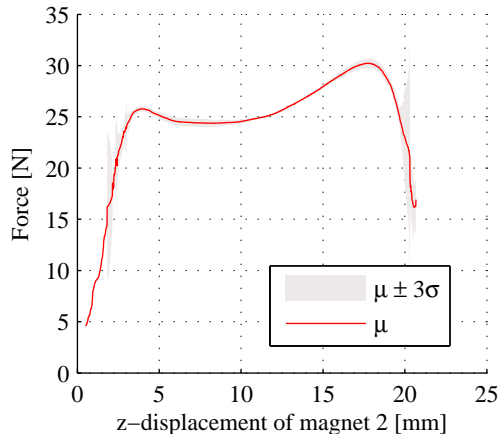
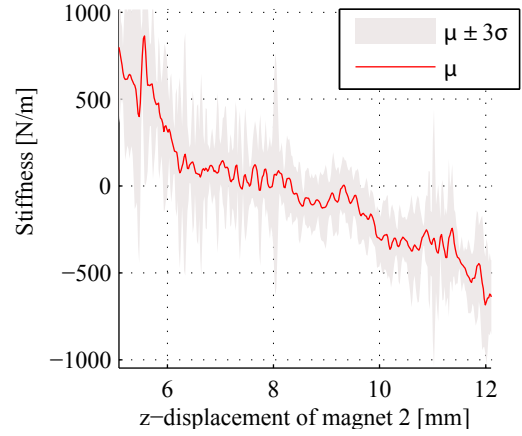
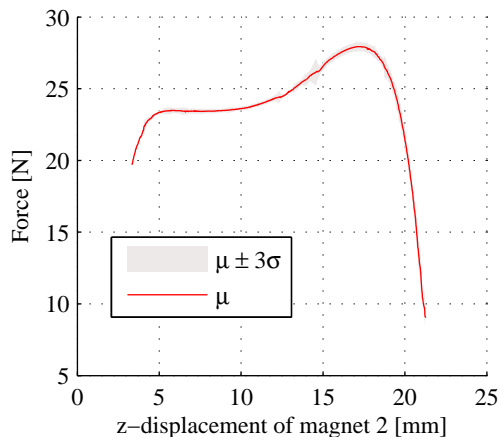
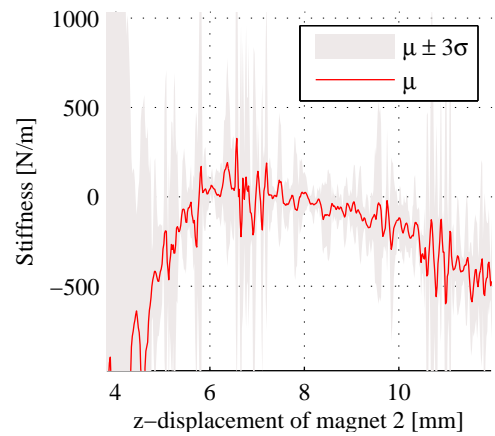
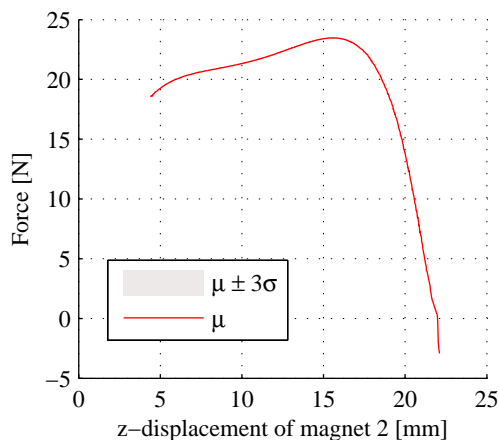
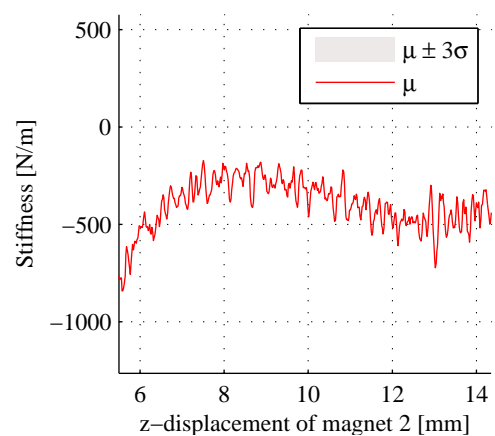
(a) Force for $d = 0.5 \pm 0.05$ mm, $\alpha = 0$ deg, $n = 6$ (b) Stiffness for $d = 0.5 \pm 0.05$ mm, $\alpha = 0$ deg, $n = 6$ (c) Force for $d = 1.0 \pm 0.05$ mm, $\alpha = 0$ deg, $n = 3$ (d) Stiffness for $d = 1.0 \pm 0.05$ mm, $\alpha = 0$ deg, $n = 3$ (e) Force for $d = 2.0 \pm 0.05$ mm, $\alpha = 0$ deg, $n = 1$ (f) Stiffness for $d = 2.0 \pm 0.05$ mm, $\alpha = 0$ deg, $n = 1$

Figure 6.9: The force–displacement characteristics at an airgap of 0.5 to 2 mm and a magnet angle of zero. The red line is the average result of n measurements.

Hysteresis

The hysteresis within the gravity compensator is measured using the setup shown in figure 6.8 and the result of the measurement is shown in figure 6.10. The top graph within figure 6.10 shows the hysteresis loop, which is measured by first decreasing the z-position (red curve) and then increasing the z-position (light blue curve) of the moving magnet. The bottom graph of the same image shows the magnitude of the hysteresis, which is the difference between the red and the light blue line. The hysteresis stays within 1% of the measured force for $1.5 < z < 19$, but increases rapidly to up to 10% for $z > 19$. A possible explanation for this large amount of hysteresis is damping within the load cell.

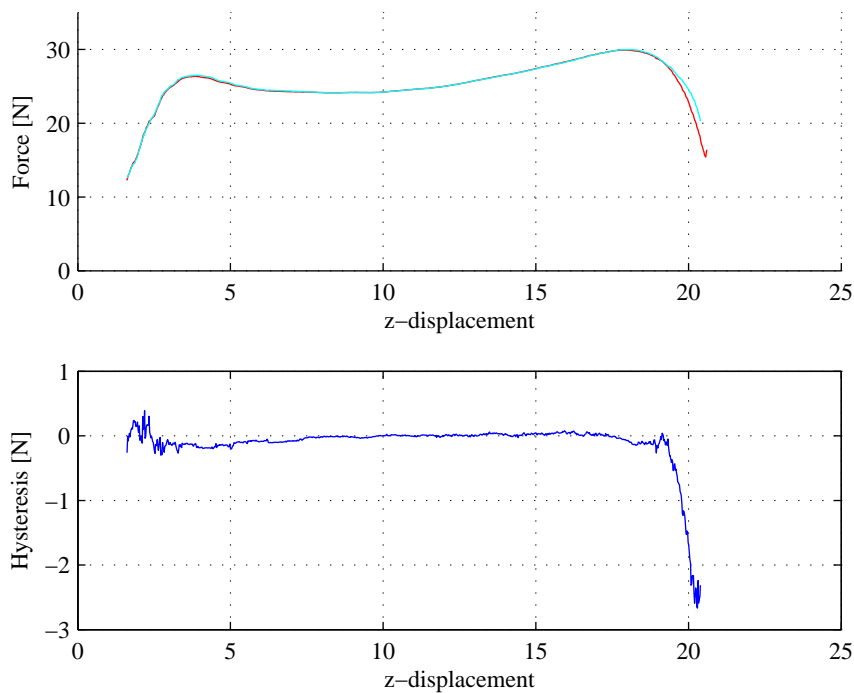


Figure 6.10: The hysteresis loop of the gravity compensator is shown in the top figure. The hysteresis is measured by first decreasing the z-position (red curve) and then increasing the z-position (light blue curve). The total the difference between the curves is shown at the bottom.

6.4 Dynamic measurements

There are three different dynamic measurements relevant to determine the performance of the setup: an eigenfrequency measurement, a damping measurement and a transmissibility measurement.

Eigenfrequency

The eigenfrequency of the system is measured using the optoNCDT laser triangulation sensor, after a force impulse had been applied to the system. The results of the measurements are shown in figure 6.11. Despite the small low stiffness and without the ability to compensate for the stiffness of the flexures, the system still achieved an 0.78 Hz eigenfrequency for vibrations with a peak to peak amplitude up to one millimeter, as is shown in figure 6.11a,b. When we would calculate the stiffness based upon the stiffness of the flexures (61 N/m) and the load

bearing capability of the magnetic spring (2500 g) we would find an eigenfrequency of 0.78 Hz, meaning that the magnetic configuration has a very low stiffness for a range of at least a one millimeter.

For larger vibrations up to two millimeters, the eigenfrequency increased to 1.17 Hz because of the non constant stiffness at the edges of the low stiffness region of the magnetic spring. This is shown in figure 6.11c,d.

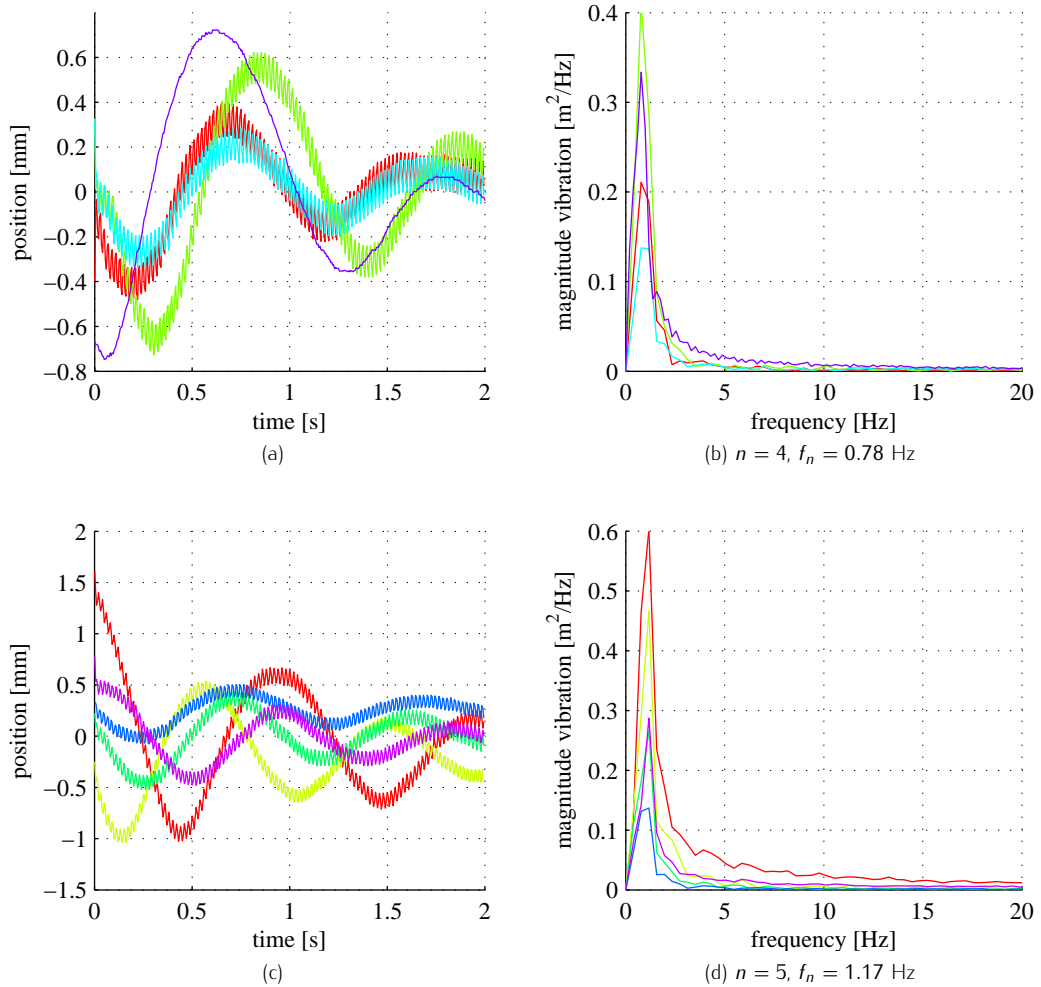


Figure 6.11: The eigenfrequency of the system is equal to (a,b) 0.78 Hz for sub-millimeter vibrations and (c,d) equal to 1.17 Hz for vibrations with a peak-to-peak amplitude of 2 mm . The measurements are sampled at 200 Hz.

Eigenfrequency pendulum

In figure 6.1 is shown that the platform is mounted below the magnetic spring by wires, forming a pendulum. One could question if the results from figure 6.11 are indeed the eigenfrequencies of the system in z-direction, or that they are the result of a crosscoupling between the pendulum motions and the z-direction.

The eigenfrequency of a pendulum is given by [29]:

$$f = \frac{1}{2\pi} \sqrt{\frac{g}{l}} \quad (6.3)$$

where l is the length from the suspension point to the center of gravity. The distance from the suspension to the bottom of the mass box is 29 cm. As the box itself is approximately 50% of the mass, l is estimated at 26 cm. According to equation (6.3) this results in a eigenfrequency of 0.98 Hz, while pendulum eigenfrequency of 0.78 Hz would require a length of 40 cm.

Eddy Current damping

The impulse response of the system—that was presented in figure 6.11—shows a vast decline in the amplitude of vibration, that was not seen during the analysis of the linear guide itself (see figure A.3 on on page 73). A longer measurement outside of the low stiffness region of the magnetic spring has been performed to create a better understanding of the rate of this decline. The result of the measurement is presented in red in figure 6.12 and shows an exponential decline.

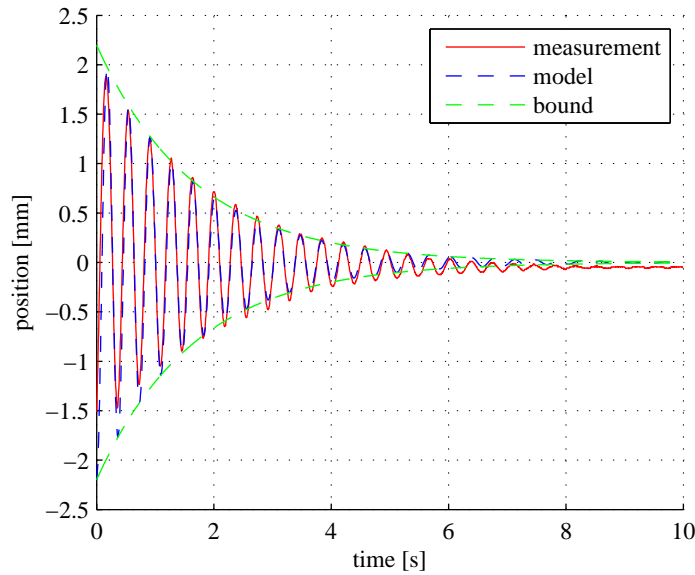


Figure 6.12: The time response of the system outside its low stiffness region shows an exponential decline in amplitude of vibration, corresponding to $\zeta = 0.6$. Sampled at 200 Hz for 10 s. The red line is the measurement, while the blue line is a fit of equation (6.4) to the measurement data.

We know that the dynamic response of a mass-spring-damper system is given by [29]:

$$z = Z_0 e^{-\zeta t} \sin(\omega t - \phi) \quad (6.4)$$

and that the harmonic motion is bounded by the $e^{-\zeta t}$ term. A damping ration of $\zeta = 0.6$ was obtained by fitting equation (6.4) to the measurement data presented in figure 6.12. As the linear guide itself has a damping ratio of $\zeta = 0.28$ (see figure A.3), the magnets must cause a significant amount of damping. The most likely explanation is that the damping is caused by eddy currents in the aluminum holder of the central magnet.

Eddy currents are the result of a changing magnetic field in a electrical conductor. According to amperes law (equation (3.9)), a changing magnetic field induces a electrical field. The magnets have a constant field, but the z -motion of the aluminum magnet holder causes a changing field in the aluminum, equal to:

$$\frac{\partial B}{\partial t} = \frac{\partial B}{\partial z} \frac{\partial z}{\partial t} \quad (6.5)$$

As result of the electric potential $\mathbf{E} = -\nabla V$, a current I_{free} starts to flow through the aluminum. The current causes heat losses equal to $P = I_{free}^2 R_{aluminum}$, that appear as viscous damping in the time response of the system.

To validate the assumption of eddy current, a non conducting magnet holder has been produced using 3D printing. Unfortunately, the dimensions of the 3D printed part were not up to the specifications, and the part could not be successfully implemented in the setup. A laser cut plexiglass magnet holder could be produced with sufficient tolerances and would solve the problem of eddy current damping, but could not been implemented due to time constraints.

6.5 Transmissibility

The transmissibility of the vibration isolation system is an important measure of its performance and can be obtained by measuring acceleration, velocity or displacements of the isolated platform relative to the surroundings (see section §2.2). As the demonstrator is a first order system, its transmissibility is fully defined by the eigenfrequency and the damping in the system. Substitution of the measured eigenfrequency and damping ratio in equation (2.9) results in the transmissibility plot of figure 6.13.

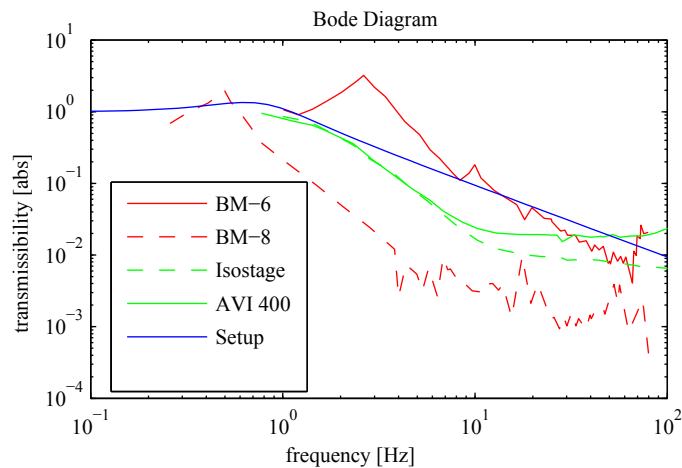


Figure 6.13: The z-transmissibility of the system (solid blue, $f_n = 0.78$, $\zeta = 0.6$). The red lines show the transmissibility of two passive minus k systems, while the green lines show the transmissibility of two high performing active systems. Data is obtained from the manufacturers websites.

Figure 6.13 shows three sets of data. The solid and dotted red lines correspond to the passive MinusK® BM-6 and BM-8 systems respectively, while the solid and dotted green lines correspond to the active Table Stable® AVI 400 and the NanoSurf® Isostage. The blue line indicates the modeled performance of the demonstrator. Although the eigenfrequency of the demonstrator is just slightly higher than the eigenfrequency of one of the best performing MinusK®system, performance is not satisfactory. The large damping ratio has an adverse effect on the transmissibility at higher frequencies, and the system is outperformed by all four systems for frequencies above 15 Hz.

6.6 Conclusions on the demonstrator

Placing the vibration isolated platform below the magnetic gravity compensator results in a stable pendulum type of system. Stability of the magnetic gravity compensator is achieved by using two leafsprings as linear guide, with a combined z-stiffness of 61 N/m. A low stiffness

in the y -direction is realized by connecting two flexure hinges to the leafsprings. Static force-displacement measurements showed a distorted force curve of the gravity compensator, with a low stiffness area of only 2-3 mm and a load bearing capacity of just 25 N, in stead of the expected 10 mm range and 40 N load bearing capacity. Dynamic measurement showed a damping ratio ζ of 0.6, which is far higher than the expected value of < 0.1 , and is caused by the eddy current damping in the aluminum and damping in the linear guide. However, there is less than 1% hysteresis in the magnetic gravity compensator and the system is stable in all directions. And even without adjusting the angle of the magnet, a sub-hertz eigenfrequency of 0.78 Hz already has been achieved.

Conclusions and recommendations

As was stated in the introduction, the goal of this research was to “*Design a passive magnetic gravity compensator, implemented in a vibration isolation system with a sub-hertz eigenfrequency*”. Objectives were to obtain and summarize the knowledge of electromagnetism required to design such a system, and use this knowledge to find a magnetic gravity compensator concept suitable for use within a passive magnetic vibration isolation system. The final objective of this research was to build a proof of concept-of-concept vertical vibration isolation system and validate that it has a sub-hertz eigenfrequency. This chapter will present the conclusions drawn from all previous chapters as well as recommendations for possible future research.

7.1 Conclusions

A vibration isolation system needs a load bearing mechanism that has a very low stiffness and contains little damping, in order to create a strong decoupling between ground vibrations and payload vibrations. Such a load bearing mechanism is called a “gravity compensator”. A passive gravity compensator can be created based upon the attractive force between magnets and iron, or on the attractive or repulsive forces between permanent magnets. The use of an “iron-free” magnetic gravity compensator concept is preferable because it has less damping due to magnetic hysteresis and eddy currents. *(based upon chapter 2, chapter 3)*

When the design of a magnetic gravity compensator contains no iron, analytical equations can be used to calculate the magnetic field and resulting forces of the permanent magnets. Analytical one- and two-dimensional solutions of the B-field were found to agree very well with COMSOL FEM simulations and measurements. Three-dimensional solutions for the magnetic fields and forces between magnets were found in literature, and could be used in future research to optimize magnetic configurations for certain force displacement curves. *(based upon chapter 3)*

It is possible to create a magnetic gravity compensator using three 20x20x5 mm square neodymium magnets with a 0.5 to 2.0 mm airgap between them. The load bearing capacity of this magnetic configuration was measured at 26 N for a 2.0 mm airgap, and its stiffness was lower than 200 N/m over a range of 10 mm. *(based upon chapter 4, chapter 5)*

COMSOL simulations show that the load bearing capacity of the magnetic gravity compensator can be increased with approximately 10N, by decreasing the airgap d between the square magnets from 2.0 to 0.5 mm. These same simulations shown the that stiffness of the gravity compensator can be adjusted from -1000 N/m to 1000 N/m by tilting the outer two magnets by an angle of -6 to 6 degrees. Combining both adjustments creates a ‘magnetic spring’ whose load bearing capacity and stiffness can be tuned mechanically. *(based upon chapter 4)*

The magnetic gravity compensator concept is implemented in a vertical vibration isolation system that is passively stable. The eigenfrequency of this system is measured at 0.78 Hz

for vibrations up to 1 mm and increases to 1.17 Hz for vibrations up to 2 mm, because of the non-constant eigenfrequency of the system. This is an vertical eigenfrequency comparable to those of top-of-the-line passive vibration isolation systems¹. The small amounts of iron present in the setup had a far larger influence on the shape of the force curve than expected and reduced the size of the low stiffness area to 2 millimeter. Due to this distorted force curve, it was impossible to validate the tunability of the stiffness with measurements. Without this force distortion, eigenfrequencies below 0.8 Hz can be achieved. *(based upon chapter 6)*

The damping ratio of the system is measured at $\zeta = 0.6$, which is an order of magnitude higher than the damping present in commercial systems, and degrades performance at higher frequencies. This high damping ratio is caused by the eddy currents induced in the aluminum magnet holder, as well as by damping in the linear guide. Solving both the problems of the distorted force curve and the eddy current damping can and should be done by changing the material choice of certain components. *(based upon chapter 6)*

The research can be called a success in that a stable passive magnetic gravity compensator with a sub-hertz eigenfrequency is build and validated. However, there is still room for improvement.

7.2 Recommendations for further research

There are a number of opportunities for future research. The current setup suffered from a distorted force curve, a high amount of damping in the linear guide, and eddy current damping in the aluminum parts. A start for a subsequent research would be to solve these problems by replacing parts of the setup by non-magnetic, non conducting materials and to redesigning the linear guide. After solving these issues, it would be possible to measure the tuning of the stiffness that has been simulated in this research. By combining the stiffness of a linear guide with equal but negative magnetic stiffness, a load bearing gravity compensator with an eigenfrequency below 0.8 Hz can be created.

A further continuation of the research could consist of designing a mechanism that can continuously adapt the tilt and y-position of the two outer magnets of the gravity compensator, so that the system can be tuned easily. Because the tilt of the two outer magnets and the airgaps between the three magnets are equal, adjusting the system should be possible with just two mechanical knobs or actuators. This way a compact low stiffness magnetic spring could be created, with a continuously tunable load bearing capacity as well as a continuously tunable stiffness.

¹However, these commercially available system isolate vibrations in all directions making their problem and vibration isolation systems far more complex than the magnetic system designed in this thesis.

Bibliography

- [1] TMC, "Technical Background," AMETEK Inc, Tech. Rep. M, 2011. [Online]. Available: www.techmfg.com/techbkgd/intro.htm
- [2] R. van den Braber, "Design of a passive inertial position sensor," Delft, p. 84, 2008.
- [3] J. Janssen, "Extended Analytical Charge Modeling for Permanent-Magnet Based Devices," Ph.D. dissertation, Eindhoven University of Technology, 2011.
- [4] —, "Design of Active Suspension using Electromagnetic Devices," Eindhoven University of Technology, Tech. Rep., 2006.
- [5] S. Hol, "Design and optimization of a magnetic gravity compensator," Ph.D. dissertation, Technische Universiteit Eindhoven, 2004.
- [6] S. Hol, E. Lomonova, and A. Vandenput, "Design of a magnetic gravity compensation system," *Precision Engineering*, vol. 30, no. 3, pp. 265–273, Jul. 2006.
- [7] R. Deng, J. Spronck, A. Tejada, and R. Munnig Schmidt, "2-DoF magnetic actuator for a 6-DoF stage with long-stroke gravity compensation." Berlin: Euspen International Conference, 2013, pp. 1–4.
- [8] R. M. Schmidt, G. Schitter, and J. van Eijk, *The design of high performance mechatronics*. Delft University Press, 2011.
- [9] C. Harris, A. Piersol, and T. Paez, *Harris' shock and vibration handbook*, 6th ed. McGraw-Hill, 2010.
- [10] MinusK, "minusK." [Online]. Available: <http://www.minusk.com/>
- [11] D. Griffiths and R. College, *Introduction to electrodynamics*, 3rd ed. Prentice Hall, 1999.
- [12] A. Zangwill, *Modern electrodynamics*, 1st ed. Cambridge University Press, 2012.
- [13] A. E. Fitzgerald and C. Kingsley, *Electric machinery*, 6th ed. McGraw-Hill, 2003.
- [14] E. P. Furlani, *Permanent Magnet and Electromechanical Devices: Materials, Analysis and Applications*. Academic Press, 2001.
- [15] L. Jabben, "Mechatronic Design of a Magnetically Suspended Rotating Platform," Ph.D. dissertation, Delft University of Technology, 2007.
- [16] H. Bleuler, "A survey of magnetic levitation and magnetic bearing types," *JSME International Journal*, vol. 35, no. 3, pp. 335–342, 1992.
- [17] D. Laro, "Mechatronic Design of an Electromagnetically Levitated Linear Positioning System using Novel Multi-DoF Actuators," Ph.D. dissertation, 2009.

- [18] Stanford University, "Green's functions." [Online]. Available: <http://www.physics.ohio-state.edu/mathur/greensfunctions.pdf>
- [19] S. D. Mathur, "Green's functions," pp. 1–6.
- [20] M. J. Hancock, "Method of Green's Functions," pp. 1–9, 2006. [Online]. Available: <http://ocw.mit.edu/courses/mathematics/18-303-linear-partial-differential-equations-fall-2006/lecture-notes/greensfn.pdf>
- [21] Supermagnete, "Calculate magnetic flux density with formula." [Online]. Available: <http://www.supermagnete.nl/eng/faq/How-do-you-calculate-the-magnetic-flux-density>
- [22] D. Vokoun, M. Beleggia, L. Heller, and P. Šittner, "Magnetostatic interactions and forces between cylindrical permanent magnets," *Journal of Magnetism and Magnetic Materials*, vol. 321, no. 22, pp. 3758–3763, Nov. 2009.
- [23] M. van Leeuwen, O. Potma, F. le Roy, and T. Speelman, "Verticale trillingsisolatie met behulp van een ferrovloeistof vlaklager," 2014.
- [24] S. Earnshaw, "On the nature of the molecular forces which regulate the constitution of the luminiferous ether," *Transactions of the Cambridge Philosophical Society*, vol. VII, no. 1, pp. 97–112, 1839.
- [25] W. Jones, "Earnshaw's theorem and the stability of matter," pp. 85–88, 2000.
- [26] S. Sabihuddin, "Potential Energy and Earnshaw's Theorem." [Online]. Available: <http://weblog.sirajs.com/article/potential-energy-and-earnshaws-theorem>
- [27] JPE Precision Point, "Knowledge Base," 2015. [Online]. Available: <http://www.jpe.nl/precisionpoint/>
- [28] H. Soemers, *Design Principles for Precision Mechanisms*, 1st ed., H. van Eerden, Ed. T-Pointprint, 2011.
- [29] S. S. Rao, *Mechanical Vibrations*, 5th ed. Prentice Hall, 2011.

Appendices

Linear guides: calculation and validation

A.1 Linear guide stiffness

The demonstrator of chapter 6 uses two spring-steel flexures as linear guide for the moving magnet. These flexures are connected to the moving body as shown in figure A.1 and have a low—but non-zero—translational stiffness k_s in the z-direction. From the schematic drawing

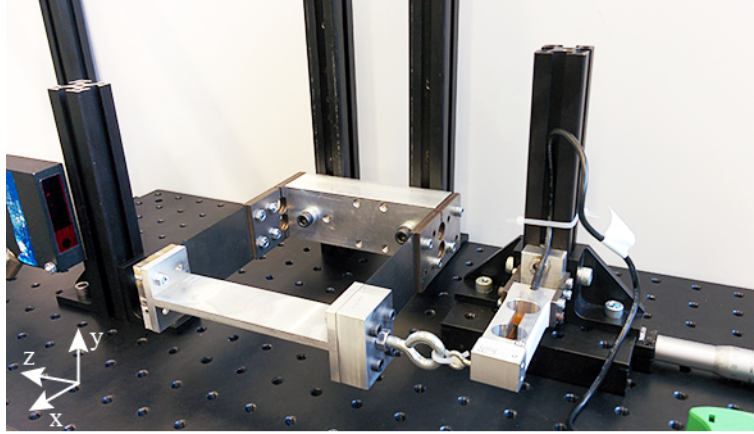


Figure A.1: Setup used to measure the stiffness of the flexures. You see two 0.2 mm thick flexures connected to the moving body, a Thorlabs stage, and optoNCDT position sensor and a Vishay load cell.

of figure 6.1 it can be seen that this stiffness adds to the stiffness of the magnets k_{mz} as:

$$k_{z,tot} = k_{sz} + k_{mz}$$

thereby influencing the performance of the system. If k_{sz} is known and smaller than 1000 N/m, we can compensate for it by adapting the angle of the magnets α , thereby creating a system with a extremely low total stiffness $k_{z,tot}$.

According to beam theory, the total stiffness of the two flexures is given by [27]:

$$k_{sx}(z) = 2 \cdot \frac{700EAJ}{L \cdot (700J + u_z^2 A)} \quad (A.1)$$

$$k_{sy} = 2 \cdot \frac{Etw^3}{L^3} \quad (A.2)$$

$$k_{sz} = 2 \cdot \frac{12EI}{L^3} \quad (A.3)$$

where t and w are the thickness and width of the flexures respectively, u_z is the z-displacement and $J = wt^2/12$ is the bending moment. The buckling force limits the minimum thickness of the flexures

$$F_{x,buckling} = 4 \frac{\pi^2 EI}{L^2} \quad (A.4)$$

and the thickness is chosen such that the flexures would not buckle under an x -alignment error of the moving body of 2 mm. A second constraint is the range of the linear guide. The maximum deflection of the flexure in z -direction is given by [27]:

$$u_z = \frac{L^2 \sigma_{max}}{3Et}$$

and is equal to half the range of the linear guide.

A manual optimization results in a flexure with a calculated stiffness of 489 N/m, whose other properties are summarized in table A.1. The calculated stiffness is validated by performing both a force measurement and a eigenfrequency analysis.

Table A.1: Properties of the flexures

w [mm]	L [mm]	t [mm]	$k_{s,z}$ [N/m]			$F_{x,buck}$ [N]	$u_{z,max}$ [mm]
			calculated	$\partial F_z / \partial z$	$m\omega^2$		
40	65	0.2	489	422	424	33.3	7.5
40	65	0.2	61	-	-	4.16	15.0

Measuring the force-displacement curve

figure A.1 shows the flexures and moving body which are connected to the 1D stage by a loads cell. When the stage is moved the displacement is measured directly at the moving body by the optoNCDT 1405-50 sensor while the force is measured using the Vishay 1006 load cell. This way, the measurement results are not influence by the strain of the connection between the moving body and the load cell. The average result and standard deviation of three force-displacement measurements are shown in figure A.2. The flexures behave as linear springs and have a stiffness of $k_{s,z} = 422$ N/m, which is found by a linear fit.

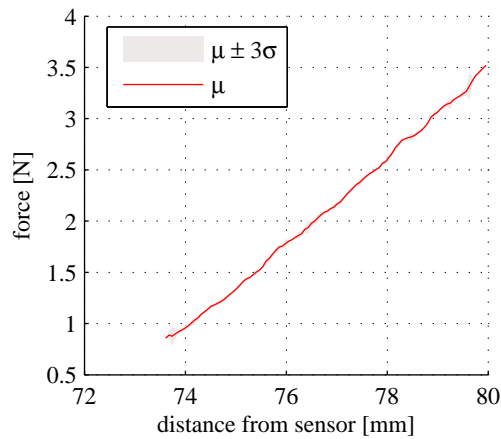


Figure A.2: The average result and 3σ standard deviation of three different force deflection measurements. The corresponding stiffness is 422 N/m

Measuring the eigenfrequency

The eigenfrequency of the system is measured using the setup shown in figure A.1, without the loadcell connected. After an initial displacement of a few millimeters, the system is released

and the displacement is measured with the optoNCDT 1402–50 sensor. The first two seconds of the time response of the system are shown in figure A.3a, while figure A.3b shows the fast Fourier transform of this signal. Using:

$$k_s = m(2\pi f_n)^2 \quad (\text{A.5})$$

we can calculate that for a mass of $m = 200$ g and an eigenfrequency of $f_n = 7.32$ Hz the flexures should have a combined stiffness of 424 N/m.

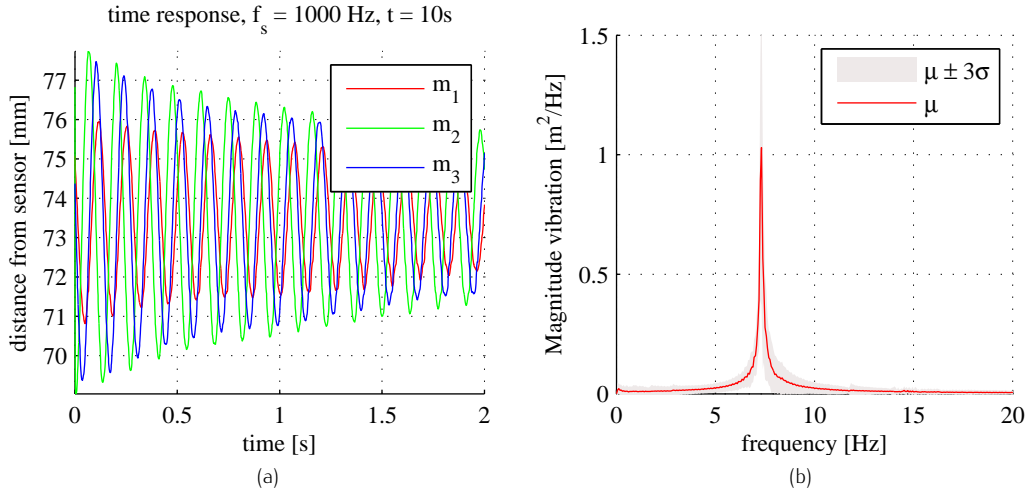


Figure A.3: The (a) time response of the system after a release from an initial displacement of ~ 4 mm and (b) the Power Spectral Density of the signal. Both figures show the eigenfrequency of 7.32 Hz. The total measurement had a length of 10 s and was sampled at 1000 Hz.

Damping coefficient

The linear guide behaves as a mass-spring-damper system, whose time response is given by [29]

$$z(t) = Z_0 e^{-\zeta t} \sin(\omega t - \phi) \quad (\text{A.6})$$

A damping ratio of 0.28 is found by fitting the time response data of figure A.3 with this equations and the bound corresponding to this data is shown in figure A.4.

Conclusion

The stiffness's obtained by the force-displacement and eigenfrequency measurements are similar as expected, but deviate 60 N/m from the calculated value. This can be explained by the fact that the stiffness is cubic proportional to the thickness—or in mathematical terms: $k_{s,z} \propto t^3$. A reduction in thickness of the flexures of 5 %—or 10 μm —already results in a stiffness of 420 N/m. The linear guide has a damping coefficient of $\zeta = 0.28$.

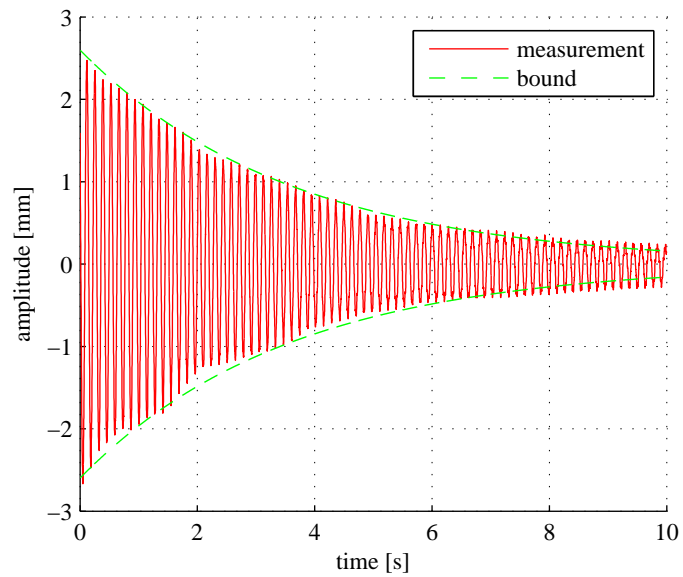


Figure A.4: The time response of the linear guide and the fitted amplitude of vibration corresponding to $\zeta = 0.28$. The data is sampled at 1000 Hz for a time span of 10 s.

Appendix B

Description of the FEM model

A number of two-dimensional and all three dimensional simulations in this thesis have been performed using COMSOL Multiphysics 4.4. Choosing the right simulation, and especially: the right mesh, saves a lot of simulation time. During this research, simulation time decreased by a factor 10 to a 100 with just some tweaking and knowing some tricks. This chapter discusses the most important ones.

B.1 Geometry of the airbox

The boundary condition of a COMSOL mfnf simulation is that the magnetic scalar potential is zero at the 'edges' of the airbox around the magnet. The size and shape of this airbox have a large influence on the calculated field. Figure B.1 shows three different airboxes. The first one is square, the second one is square with a Infinite Element Domain (IED) and the third one is round with an infinite element domain. A round airbox with an IED gives the best results.

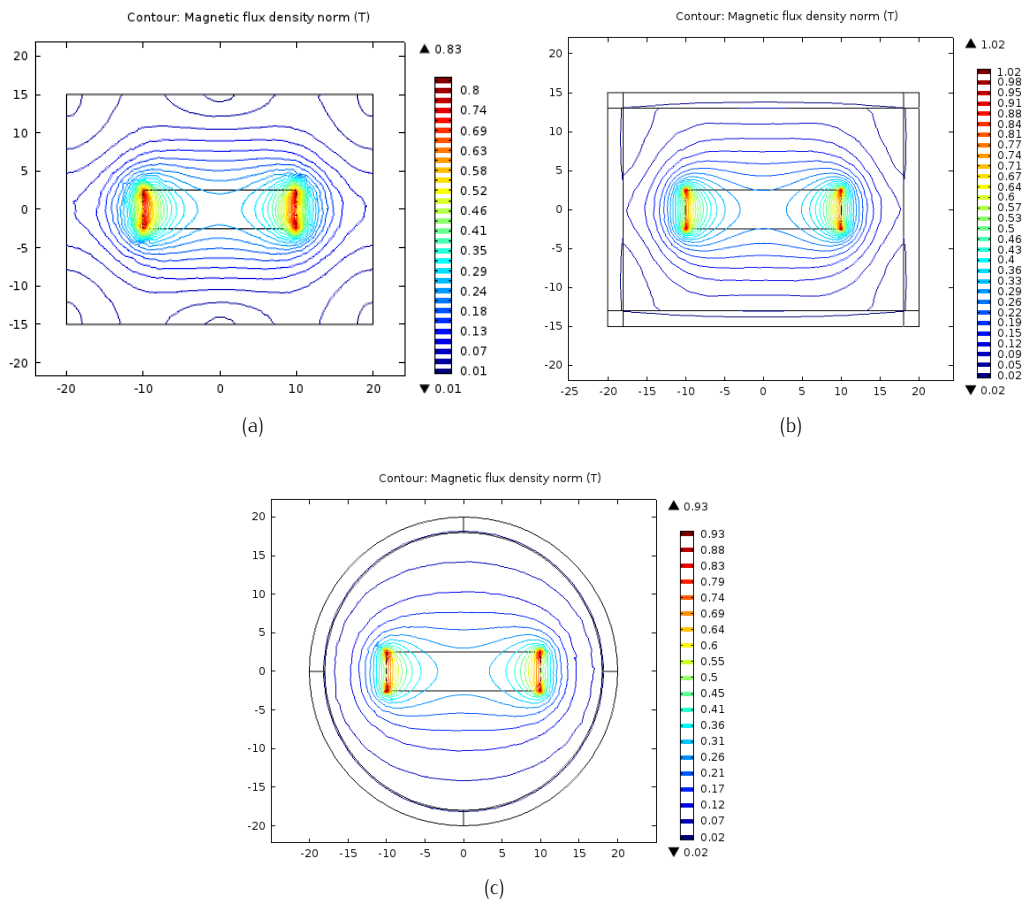


Figure B.1: Three COMSOL magnetic field no current (mfnf) simulation of a three-dimensional magnet. A round airbox with an infinite element (c) domain gives by far the best results.

B.2 Mesh

The mesh needs to be finest where the field changes most, while it can be really coarse in the infinite element domain as can be seen in figure B.2. The magnetic field changes most at the edges of the magnet, so we want the mesh finest over there. This happens automatically when you give the edges of the magnet a small radius. The air is meshed with a normal triangular mesh, while a square mesh works well for the infinite element domain.

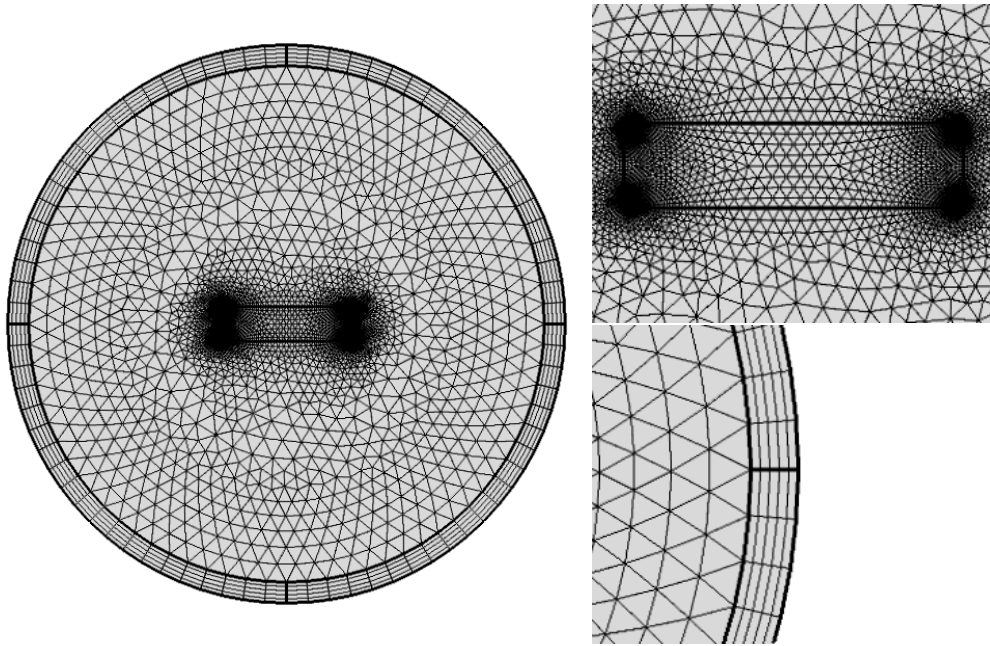


Figure B.2: Mesh of a magnetic simulation.